Symmetry-breaking patterns, tricriticalities, and quadruple points in the quantum Rabi model with bias and nonlinear interaction

Zu-Jian Ying ●[*]

School of Physical Science and Technology, and Lanzhou Center for Theoretical Physics, Lanzhou University, Lanzhou 730000, China

Quantum Rabi model (QRM) is fascinating not only because of its broad relevance but also due to its few-body quantum phase transition. In practice, both the bias and the nonlinear coupling in QRM are important controlling parameters in experimental setups. We study the interplay of the bias and the nonlinear interaction with the linear coupling in the ground state which exhibits various patterns of symmetry breaking and different orders of transitions. Several situations of tricriticalities are unveiled in the low-frequency limit and at finite frequencies. We find that the full quantum-mechanical effect leads to transitions, tricriticalities, quadruple points, and a fine structure of spontaneous symmetry breaking, which are much beyond the semiclassical picture. We clarify the underlying mechanisms by analyzing the energy competitions and the essential changeovers of the quantum states, which enables us to extract most analytic phase boundaries.

I. INTRODUCTION

In the past decade, both experimental [1] and theoretical [2,3] progresses have brought the strong light-matter interaction to the frontiers of quantum optics and quantum physics. The experimental access to increasingly larger coupling strengths has opened a regime with a rich phenomenology [1,4] unexpected in weak couplings. Beyond the Jaynes-Cummings model [5], which is valid in weak couplings, the quantum Rabi model (QRM) [6] is the most fundamental model for strong light-matter interaction. The QRM also has a wide relevance, being a fundamental building block for quantum information and quantum computation [1,7–10], closely connected to models in condense matter [4], and even applied in black hole physics [11]. Theoretically, the milestone work of revealing Braak integrability [2] for the QRM has not only heated up the interest in the light-matter interaction but also triggered an intense dialogue between mathematics and physics [3,12–42].

The fast experimental advances have pushed the coupling strength all the way through from weak-, strong-coupling regimes to ultrastrong-coupling regime and even beyond [1,43–54]. A most fascinating consequence of continuing enhancements of the coupling strength is the emergence of phase-transition-like phenomena [19–22,24–27,55]. As a usual impression, phase transitions mostly occur in thermodynamical limit in condensed matter. Note that the QRM is composed of a single qubit or spin-half system in coupling with a light field or a bosonic mode, thus the few-body quantum phase transition found in the QRM appears quite particular. Interestingly via the scaling relation of the critical behavior it has been established that the few-body phase transition can be can be bridged to the phase transition in the thermodynamic limit [21].

Along with the continuing regime expanding of the QRM in the frontiers of quantum optics and quantum physics, a playground for physics in nonlinear quantum optics is also opened by an extended version of the QRM, so-called two-photon quantum Rabi model [23,56–63]. The conventional QRM is a linear model in the sense that it is via a single-photon process of absorption and emission for the qubit or spin-half system to couple with a bosonic mode. The interaction in the two-photon model involves a coupling via two-photon process of absorption and emission, which is nonlinear. Recently the nonlinear two-photon interaction has attracted an increasing attention as the model can be implemented in trapped-ion systems [58,59] and superconducting circuits [56,57] with the interaction strength enhanced to realize the ultrastrong regime. Critical behavior also appears in such two-photon QRM and a special phenomenon is the spectral collapse [58,61–63], i.e., its discrete spectrum collapses into a continuous band when the nonlinear interaction strength approaches to the critical point. It has been noticed that the spectral collapse can be tuned from incomplete collapse to complete collapse by variation of the system frequency [23].

An important character of the QRM noteworthy to mention is the symmetry. It is well-known that the QRM has the so-called parity symmetry. Generally speaking, it is quite common that only at certain parameter point can a physical system possess a symmetry and one needs very fine-tuned conditions to maintain the symmetry, while the realistic conditions in experimental setups may break the symmetry. Nevertheless, although symmetry is the diamond of physics, what makes the world of physics really rich is often the symmetry breaking. As far as the QRM in the light-matter interaction is concerned, it is known that anisotropy [17,21] in the coupling will preserve the parity symmetry. However,

----

[*]yingzj@lzu.edu.cn

the existence of a bias or a nonlinear interaction will definitely break the parity symmetry of the linear QRM. Despite that a pure two-photon model also has a parity symmetry, the mixture of the single-photon coupling and two-photon interaction will break both the parity symmetries of the linear QRM and of the two-photon QRM. In such a mixed case novel phenomena could arise, such as the emergence of triple point and spontaneous symmetry breaking [24]. Recently there is a trend of growing interest in the mixed model [24,64–67]. So far, most studies have been focusing on the mixed model without taking the bias into account, however in realistic conditions of experimental setups it is more general to have both the bias and nonlinear interaction in the presence [68]. In such a situation a full knowledge of the competition and interplay of the bias and nonlinear interaction is still lacking and very desirable.

In this work we present a systematic study on a general realistic model [56,68,69] composed of the linear coupling, the bias, the nonlinear interaction as well as a nonlinear Stark term. We focus on the ground state which exhibits various patterns of symmetry breaking and different orders of phase transitions. We find that in such a realistic model tricritical-like behavior can be induced in diverse situations. It is also interesting to get a contrast of semiclassical picture in the low-frequency limit and the full quantum-mechanical effect at finite frequencies. We demonstrate that the quantum-mechanical effect leads to a much richer phenomenology, including transitions, tricriticalities, and quadruple points.

The paper is organized as follows. In Sec. II we introduce the general model with bias and nonlinear interaction. In Sec. III we give a primary description of the methods applied in the present work. Different transition orders are interpreted by variational energy in Sec. IV. The parity symmetry of the conventional QRM is addressed in Sec. V and different patterns of symmetry breaking are shown in Sec. VI in the presence of bias and nonlinear interaction. In Sec. VII we present the full phase diagrams in low-frequency limit, in the respective or simultaneous presence of the bias and the nonlinear interaction, together with obtained analytic boundaries. In the low-frequency limit we reveal a first tricriticality in Sec. VIII. In Sec. IX we discuss the finite-frequency case, unveiling more situations of tricriticalities. We show that there could be three, even four successive transitions, the analytic phase boundaries are also presented. Quadruple points are demonstrated in Sec. X. In Sec. XI, we discuss how the ground-state wave function changes at the various phase transitions. Section XII is devoted to clarify the mechanisms underlying the various symmetry-breaking patterns and successive transitions. We address the semiclassical picture and the full quantum mechanics effect, the latter leading to more phase transitions and thus being the origin of the various tricriticalities and quadruple points. We explain why different quantities respond to the transitions differently. We also show the scaling of the Stark term in the nonlinear interaction. Section XIII provides brief derivations of the analytic boundaries. In the final section we summarize the results and discuss the realization regime for experimental parameters in superconducting circuit systems.

II. MODEL

Besides the linear coupling of the QRM, experimental setups in superconducting circuits actually involve both nonlinear coupling and bias, with a Hamiltonian reading as [56,68]

$$
\begin{aligned}
H &= H_0 + H_t + H_\epsilon, \\
H_0 &= \omega a^\dagger a + \frac{\Omega}{2}\sigma_x + g_1\sigma_z(a^\dagger + a), \\
H_t &= g_2\sigma_z[(a^\dagger)^2 + a^2 + \chi\widetilde{n}], \quad H_\epsilon = -\epsilon\sigma_z,
\end{aligned}
\tag{1}
$$

where $\sigma_{x,y,z}$ is the Pauli matrix, $a^\dagger(a)$ creates (annihilates) a bosonic mode with frequency ω. The Ω term is atomic level splitting in cavity systems, while in the superconducting circuit systems it is tunneling between the spin-up and spin-down states of the flux qubit [70] as represented by σ_z. Following Ref. [15], we adopt the spin notation in the superconducting circuit systems which can realize very strong couplings.

The conventional QRM is described by H_0 where the coupling is linear, via the single-photon process of absorption and emission, with a coupling strength g_1. The nonlinear interaction is denoted by H_t with the coupling strength g_2. Here we have included a Stark-like term [37,56], $\chi\widetilde{n}$ with $\widetilde{n} = a^\dagger a + aa^\dagger$ essentially being the photon number, to retrieve the conventional two-photon form [56] by $\chi = 0$ and the quadratic form $(a^\dagger + a)^2$ in experimental setups [68] by $\chi = 1$. One can also obtain a pure Stark-like term by setting $g_2 \to 0$ while keeping χ inversely proportional to the bare nonlinear interaction $\chi \propto 1/g_2$. It turns out that for the properties discussed in present work the Stark-like term contributes to a scaling factor and by

$$
\widetilde{g}_2 = (1 + \chi)g_2
\tag{2}
$$

we get similar results. For simplicity, unless otherwise mentioned, we use g_2 to represent general $\widetilde{g}_2$ throughout the figures. The origin of the scaling will be clarified in Sec. XII B. Here it should be mentioned that the Stark-like term in the superconducting circuits under consideration [56,68] involves σ_z rather than σ_x in the conventional Stark term [37,40] which may have a different scenario and we shall address elsewhere. Hereafter, we define

$$
g_s = \sqrt{\omega\Omega}/2, \qquad g_t = \omega/2,
\tag{3}
$$

as the scale references for the strengths of linear coupling g_1 and nonlinear interaction g_2. Actually g_s is the critical point for the QRM H_0 [19,20,27,55] and g_t is the critical value for the two-photon quantum Rabi model [23,56–63].

The last term H_ϵ denotes the bias. For a flux qubit in superconducting circuit systems, the Josephson potential energy as a function of junction phase difference has a double-well structure which contributes to the two qubit states [70]. When the two wells are symmetric the two qubit states are degenerate, in this case there is no bias. The degeneracy of the two qubit states can be raised by introducing the bias term which can be tuned by an external flux and a bias current [68].

III. METHODS

To see the exact behavior of the model we use exact diagonalization to figure out the ground-state phase diagrams, while to gain some physical insights we shall apply semiclassical picture in the low-frequency limit and the polaron picture at finite frequencies. For the semiclassical picture and the polaron picture we give a primary description in this section, while applications for interpretation of transition orders, mechanism analysis and derivations of analytic boundaries are left in Secs. IV, XII, and XIII.

A. Upper and lower cutoffs in exact diagonalization

The exact diagonalization can be carried out by expanding the wave function on the basis $|n, \sigma_z\rangle$,

$$|\psi\rangle = |\psi_+\rangle + |\psi_-\rangle = \sum_{n=0}^{\infty} (c_{n,+}|n, +\rangle + c_{n,-}|n, -\rangle), \tag{4}$$

where $+ (-)$ labels the up $\uparrow$ (down $\downarrow$) spin in z direction and n is the quantum number for the eigenstate of quantum harmonic oscillator (as a representation of the bosonic mode). On the basis the Hamiltonian can be written as a symmetric $n \times n$ matrix,

$$\begin{pmatrix} \varepsilon_0^+ & \frac{\Omega}{2} & g_1 & 0 & \sqrt{2}g_2 & 0 & \cdots \\ \frac{\Omega}{2} & \varepsilon_0^- & 0 & -g_1 & 0 & -\sqrt{2}g_2 & \cdots \\ g_1 & 0 & \varepsilon_1^+ & \frac{\Omega}{2} & \sqrt{2}g_1 & 0 & \cdots \\ 0 & -g_1 & \frac{\Omega}{2} & \varepsilon_1^- & 0 & -\sqrt{2}g_1 & \cdots \\ \sqrt{2}g_2 & 0 & \sqrt{2}g_1 & 0 & \varepsilon_2^+ & \frac{\Omega}{2} & \cdots \\ 0 & -\sqrt{2}g_2 & 0 & -\sqrt{2}g_1 & \frac{\Omega}{2} & \varepsilon_2^- & \cdots \\ 0 & 0 & \sqrt{6}g_2 & 0 & \sqrt{3}g_1 & 0 & \ddots \\ 0 & 0 & 0 & -\sqrt{6}g_2 & 0 & -\sqrt{3}g_1 & \\ \vdots & \vdots & \vdots & \vdots & \vdots & \vdots & \vdots \end{pmatrix},$$

where $\varepsilon_n^{\sigma_z} = n\omega - \sigma_z\epsilon + \sigma_z(2n + 1)\chi g_2$. In principle, the wave function expansion and the Hamiltonian matrix involve an infinite number of n. Nevertheless, since we are focusing on the ground state, as usual one can introduce an upper cutoff n_{max} which should guarantee the numerical convergence with a required accuracy. The upper cutoff n_{max} will grow with the coupling strengths g_1, g_2 and also depends on the frequency. For a strong coupling a lower frequency requires a larger n_{max}, e.g., at $\omega = 0.001\Omega$ the upper cutoff may be several thousands for a coupling strength g_1 in a range $[1g_s, 3g_s]$. It may be worthwhile to mention that one can also apply a lower cutoff n_{min} to reduce the computational cost in strong couplings, since the distribution of the basis weight c_{n,σ_z} has a peaklike profile in strong couplings and the basis weight for small n may also become negligible as large n, as illustrated by Fig. 1.

In the present work we focus on the ground-state properties. With the ground state obtained by exact diagonalization, one can calculate the physical expectations over the ground state

$$\langle \hat{O} \rangle = \langle \psi | \hat{O} | \psi \rangle, \qquad \langle \hat{O} \rangle_\sigma = \langle \psi_\sigma | \hat{O} | \psi_\sigma \rangle, \tag{5}$$

where $\hat{O}$ is an operator and the wave function has been normalized by $\langle \Psi | \Psi \rangle = 1$. We will investigate various physical quantities, including $\langle \sigma_z \rangle$, $\langle \sigma_x \rangle$, $\langle \hat{x} \rangle$, and $\langle \hat{x} \rangle_\sigma$, where $\hat{x} = (a^\dagger + a)/\sqrt{2}$, which are sensitive to different transitions.

B. Effective spatial coordinate representation

To facilitate the understanding in further discussions we rewrite the bosonic mode in the model Hamiltonian in terms of the quantum harmonic oscillator. By the transformation $a^\dagger = (\hat{x} - i\hat{p})/\sqrt{2}$, $a = (\hat{x} + i\hat{p})/\sqrt{2}$, we transfer to the space of the effective position $\hat{x}$ and the momentum $\hat{p}$. Thus, the Hamiltonian takes the form

$$H = \sum_{\sigma_z = \pm} \left(h^{\sigma_z} |\sigma_z\rangle\langle\sigma_z| + \frac{\Omega}{2}|\sigma_z\rangle\langle\overline{\sigma}_z| \right), \tag{6}$$

which is composed of the effective free-particle part (the h^{σ_z} term) and tunneling part (the Ω term). Here $\overline{\sigma}_z = -\sigma_z$ labels the spin as in Eq. (4). The effective free-particle Hamiltonian in the spin components can be rearranged to be

$$h^\pm = \omega \left(\frac{\hat{p}^2}{2m_\pm} + v_\pm \right) + e_0, \qquad v_\pm = v_\pm^{hp} + b_\pm + b_0 \mp \epsilon, \tag{7}$$
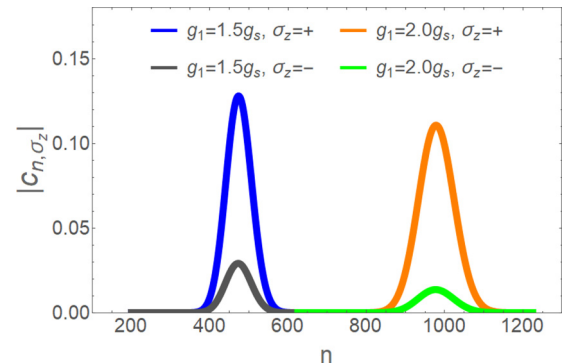
FIG. 1. Distribution of basis weight $C_{n,\sigma}$ (plotted by absolute value) in exact diagonalization for linear coupling strengths $g_1 = 1.5g_s$ and $g_1 = 2.0g_s$, at bias $\epsilon = 0.5g_t$ and nonlinear interaction $g_2 = -0.02g_t$ and frequency $\omega = 0.001\Omega$. Here we have defined $g_s = \sqrt{\omega\Omega/2}$ and $g_t = \omega/2$.

where

$$v_{\pm}^{hp} = \tfrac{1}{2}m_{\pm}\varpi_{\pm}^2[x - x_{0,\pm}]^2, \qquad (8)$$

$$b_{\pm} = \pm\frac{\widetilde{g}_2 g_1'^2}{2\left(1 - \widetilde{g}_2^2\right)}, \qquad (9)$$

$$b_0 = -g_1'^2/[2\left(1 - \widetilde{g}_2^2\right)]. \qquad (10)$$

We have defined $g_1' = \sqrt{2}g_1/\omega$, $g_2' = 2g_2/\omega$ and $e_0 = -\omega/2$. Here $m_{\pm} = (1 \mp g_2' \pm \chi g_2')^{-1}$ is the effective mass and $\varpi_{\pm} = [(1 \pm \chi g_2')^2 - g_2'^2]^{1/2}$ is frequency renormalization. The $x_{0,\pm} = \mp g_1'/(1 \mp \widetilde{g}_2)$ is the potential displacement for the potential bottom shifting horizontally from the origin, while b_0 is the vertical shift which is both downward for the two spin components. In this picture we see the different roles played by the physical parameters of the model: the linear coupling g_1 separates the potentials of the two spin components, the bias ϵ shifts the potentials downwards or upwards oppositely for the two spin components, while the nonlinear interaction g_2 not only leads to asymmetry in frequency $\varpi_{\pm}$ and potential displacement $x_{0,\pm}$ but also results in the vertical potential difference $b_{\pm}$.

In this representation we can apply a variational method such as the polaron picture by decomposing the ground-state wave function into four wave packets [20],

$$|\psi\rangle = (\alpha^+\varphi_{\alpha}^+ + \beta^+\varphi_{\beta}^+)|\uparrow\rangle + (\alpha^-\varphi_{\alpha}^- + \beta^-\varphi_{\beta}^-)|\downarrow\rangle, \quad (11)$$

where $\varphi_{\alpha}^{\pm}$ corresponds to polaron and $\varphi_{\beta}^{\pm}$ represents antipolaron induced by tunneling effect, $\alpha^{\pm}$ and $\beta^{\pm}$ are weight coefficients. Practically $\varphi_{\alpha}^{\pm}$ and $\varphi_{\beta}^{\pm}$ can be approximated by the ground states of quantum harmonic oscillators with optimized displacements and frequency renormalizations.

We shall apply the polaron picture to provide an understanding for the various phase transitions, explain why the quantities $\langle\sigma_z\rangle$, $\langle\sigma_x\rangle$, $\langle\hat{x}\rangle$, and $\langle\hat{x}\rangle_{\sigma}$, respond differently to the transitions, and extract analytic phase boundaries at finite frequencies.

C. Semiclassical energy in low-frequency limit

Semiclassical picture can provide a good description for the transitions in the low-frequency limit. This can be seen from a scale estimation of either the wave-packet size or the contribution of the kinetic energy.

In fact, the ground-state wave function basically can be decomposed into ground states of quantum harmonic oscillators with displacement and frequency renormalizations [20]. The wave-packet size is of order 1 in the aforerepresented dimensionless formalism. The potential size, represented by the distance of the potential bottoms in two spins, at phase transitions can be estimated by $x_{0,\pm}$, being of order $g_s = \sqrt{2}g_s/\omega \propto \sqrt{\Omega/\omega}$. Thus, the ratio between the wave-packet size and the potential size is of order $\sqrt{\omega/\Omega}$ which becomes smaller at a lower frequency. In the low-frequency limit, $\omega/\Omega \to 0$, with the wave-packet size relatively negligible, one can regard the effective particle as a classical mass point in the effective spatial space, without a spatial structure of probability distribution as in quantum mechanics. Thus, the spatial part can be treated as a classical part. However we keep the leading tunneling effect in the spin space, which

is quantum part. In such a semiclassical consideration, the ground state is motionless with a vanishing kinetic energy ($p^2 = 0$).

We can also draw the same conclusion from the quantum mechanical consideration of the kinetic energy. This can been seen from an order estimation of the contribution of the kinetic energy. We take the transition of the QRM as an example. The transition occurs at $g_1 = g_s$ and before the transition the particle resides around the origin $x = 0$ to gain a maximum tunneling energy. In such a situation the potential energy is of an order $\omega v_{\pm}^{hp} \sim \omega[g_s']^2 = \omega[\sqrt{2}g_s/\omega]^2 \propto \Omega$, which is indeed competing with the the tunneling energy to give rise to the transition. Note that the kinetic energy is of an order ω, like the quantum harmonic oscillator, which in the low-frequency limit becomes negligible relatively to the order of the potential energy and tunneling energy. Thus, in the low-frequency limit we can set $\hat{p}^2 \to 0$, which is equivalent to the semiclassical ground-state energy for a quantum particle (spin space) in a classical external potential (effective spatial part).

We can get the variational energy readily in the above semiclassical picture. The spin part can be formulated in the following eigenequation in matrix form,

$$\begin{pmatrix} \varepsilon_+ & \frac{\Omega}{2} \\ \frac{\Omega}{2} & \varepsilon_- \end{pmatrix}\begin{pmatrix} \beta^+ \\ \alpha^- \end{pmatrix} = \varepsilon\begin{pmatrix} \beta^+ \\ \alpha^- \end{pmatrix}, \qquad (12)$$

where $\varepsilon_{\pm} = \omega v_{\pm} + \varepsilon_0$ has a zero kinetic energy. The eigenenergy for the ground state is determined by

$$\varepsilon = \tfrac{1}{2}[(\varepsilon_+ + \varepsilon_-) - \sqrt{(\varepsilon_+ - \varepsilon_-)^2 + \Omega^2}]. \qquad (13)$$

Note $\varepsilon = \varepsilon(x)$ is a function of the spatial position x as $v_{\pm}$ is position dependent, one also needs to minimize the energy in the spatial part by

$$\frac{\partial \varepsilon(x)}{\partial x} = 0, \qquad (14)$$

which decides the final ground-state energy in the semiclassical picture. This variational energy provides a convenient analysis for transition orders and also enables us to obtain the analytic phase boundaries in the low-frequency limit.

IV. DIFFERENT ORDERS OF PHASE TRANSITIONS

The QRM H_0 has a phase transition at $g_1 = g_s$ in the low-frequency limit [19,20,27,55]. This phase transition is of second order. With the additional competitions from the nonlinear interaction and the bias our model H will involve different orders of transitions. These different order transitions can be readily seen from the energy competition in the semiclassical picture. In Fig. 2 we illustrate the semiclassical variational energy as a function of x before transitions [blue (upper) solid lines], at transitions [black (middle) dashed lines] and after transitions [orange (lower) solid line] in different situations.

Figure 2(a) presents the case of the conventional QRM without the bias and the nonlinear interaction. Before the transition at $g_1 = g_s$ the energy minimum is located at the origin, after the transition the origin becomes an unstable saddle point while the ground state lies in the formed two symmetric minima which are moving away from the origin. At the transition point the minimum bottom becomes flat
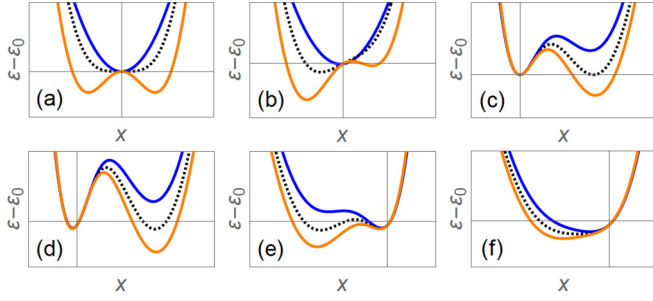
FIG. 2. Energy competitions and transition orders. Semiclassical variational energy ε before [blue (upper) solid lines], at [black (middle) dotted lines] and after [orange (lower) solid lines] transitions, with respect to the effective particle position x for (a) $\epsilon = 0$ and $g_2 = 0$, (b) $\epsilon \neq 0$ and $g_2 = 0$, (c) $\epsilon = 0$ and $g_2 \neq 0$, (d) $\epsilon \neq 0$ and $g_2 > 0$, (e) $\epsilon \neq 0$ and $g_2 < 0$ nearby $|g_2| = |g_t|$, (f) $\epsilon \neq 0$ and $g_2 < 0$ nearby $g_2 = 0$. Here $\varepsilon_0 = -(\omega + \Omega)/2$. (The actual plotting parameters are (a) $\epsilon = 0$, $g_2 = 0$, and $g_1/g_s = 0.5$, 1.0, 1.1; (b) $\epsilon = 0.015\Omega$, $g_2 = 0$, and $g_1/g_s = 0.5$, 1.0, 1.1; (c) $\epsilon = 0$, $g_2 = 0.7g_t$ and $g_1/g_s = 0.695$, 0.714, 0.729; (d) $\epsilon = 0.05\Omega$, $g_2 = 0.7g_t$, and $g_1/g_s = 0.748$, 0.767, 0.782; (e) $\epsilon = 0.05\Omega$, $g_2 = -0.7g_t$, and $g_1/g_s = 0.648$, 0.667, 0.682; (f) $\epsilon = 0.05\Omega$, $g_2 = -0.5g_t$, and $g_1/g_s = 0.765$, 0.784, 0.799. We set $\omega = 0.001\Omega$ and $\Omega = 1$ is taken as the unit and x is dimensionless as indicated by the transformation $\hat{x} = (a + a^\dagger)/\sqrt{2}$.)

with a vanishing second derivation $\partial^2\varepsilon/\partial x^2 = 0$. Although the transition turns the minimum number from one to two, this transition is continuous as two minimum positions separate continuously from the origin.

The presence of the bias breaks the symmetry in the energy profile in any regime of the linear coupling, as illustrated in Fig. 2(b). The profile difference of single minimum and double minima in energy leads to different response to the bias before and after the transition. Before the transition point g_s the energy has no competition as the single minimum is the only choice. With the bias this single minimum moves gradually away from the origin. After the transition, there are two minima which are degenerate in the absence of the bias. Any tiny strength of bias will immediately break the symmetry and raise the degeneracy. Changing the sign of the bias the ground state will shift from one side of the minimum to the other side. Either the bias opening or a sign change will lead to an abrupt jump in polarization, leading to a discontinuous first-order transition.

The scenario of energy competition is different in the presence of nonlinear interaction, as demonstrated in Fig. 2(c). There are two local energy minima both before and after the transition [here the transition moves from g_s to g_{1c} in Eq. (15)], one at the origin, the other away from the origin. Before the transition, the ground state lies in the minimum at the origin while the other local minimum is higher in energy. At the transition the higher minimum is lowered to get degenerate with the one at the origin. After the transition, the energy preference gets reversed and the ground state turns to the lower minimum away from the origin. Note that, in a sharp contrast to the continuous variation of the minimum position in Fig. 2(a), the transition here in Fig. 2(c) is companied with a sudden shift of minimum position. This

discontinuous shift of minimum position results in a first-order transition.

In the presence of both the bias and the nonlinear interaction, there are three situations which should be distinguished. Figure 2(d) shows the first case in which the bias ϵ and the nonlinear interaction g_2 have the the same sign. In his case the bias pushes the minimum at the origin away to the opposite side of the higher minimum. In this case the transition also is discontinuous (first-order), similar to Fig. 2(c). Figure 2(e) shows the second case with the sign of g_2 opposite to ϵ and the amplitude of g_2 closer to g_t. In this case the two energy minima are located on the same side but still far away enough to have a barrier between them. Thus, the transition also has a discontinuous shift of the minimum position, being first-order. The third situation shown in Fig. 2(f) still has opposite signs of g_2 and ϵ but with a small amplitude of g_2. In this case the two local energy minima are too close to have a barrier to separate them explicitly. Although the minimum position may have a quick shift but the variation is continuous. Thus, the first-order transition is softened, being second-order-like or even fading away.

V. PARITY SYMMETRY OF THE QRM

The conventional QRM H_0 possesses the parity symmetry $\hat{P} = \sigma_x(-1)^{a^\dagger a}$ which commutes with H_0. The parity operation $\hat{P}$ simultaneously reverses the spin sign and inverses the effective spatial space $x \to -x$. The spin sign reversion can be seen directly from $\sigma_x = (\sigma^+ + \sigma^-)$. The space inversion can be conveniently shown by expanding the wave function on the basis of quantum harmonic oscillator as in Eq. (4). Then the action of the parity operation leads to $\hat{P}|\psi\rangle = \sum_{n=0}^{\infty}(-1)^n(c_{n,+}|n,-\rangle + c_{n,-}|n,+\rangle)$. In the spatial coordinate it means the transform

$$\hat{P} : \psi_\pm(x) \to \sum_n (-1)^n c_{n,\mp}\phi_n(x)$$

$$= \sum_n c_{n,\mp}\phi_n(-x) = \psi_\mp(-x),$$

where we have applied the fact that the eigenstate of quantum harmonic oscillator, $\phi_n(x)$, is an odd (even) function of x for an odd (even) quantum number n. Thus, we see the space inversion $x \to -x$, besides the spin reversion. The parity symmetry requires $\psi_\pm(x) = P\psi_\mp(-x)$ where $P = \pm 1$. The ground state of QRM has a parity $P = -1$. Apparently, either in the negative or positive parity symmetry, the spin expectation $\langle\sigma_z\rangle$ along z direction is vanishing, which is a characteristic of the parity symmetry. In the present work we focus on the symmetry breaking in the ground state of the general model H with the bias, the nonlinear interaction and the Stark coupling.

VI. DIFFERENT PATTERNS OF SYMMETRY BREAKING

Either the bias or the nonlinear interaction will break the parity symmetry of the linear QRM H_0. Interestingly different scenarios arise in the interplay of linear coupling with the bias and the nonlinear interaction, leading to various patterns of symmetry breaking. On the one hand, the linear QRM has a critical point at $g_1 = g_s$ which also turns out to be a critical
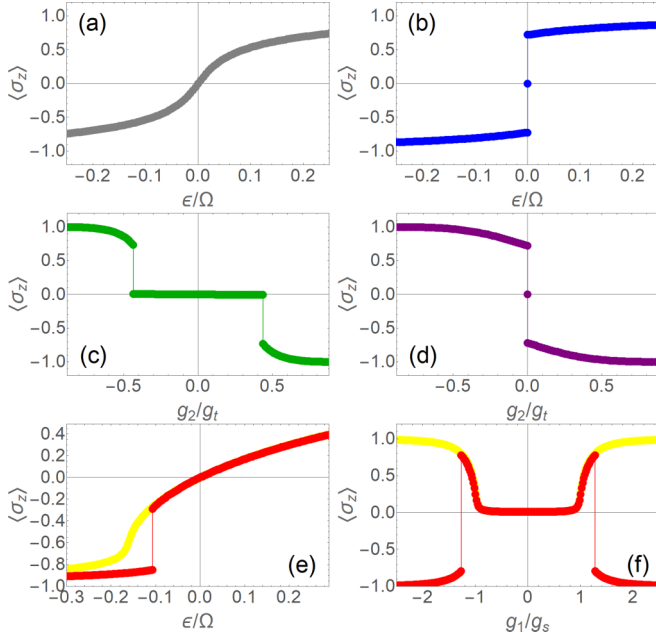
FIG. 3. Different patterns of symmetry breaking. (a–f) Spin expectation $\langle\sigma_z\rangle$ in the cases of (a) paramagnetic-like, (c) antiferromagnetic-like, (b, d) the spontaneous symmetry breaking, (e) paramagnetic+first- or second-order-transition, and (f) antiferromagnetic+first- or second-order-transition. These cases are illustrated by fixed parameters at $g_2 = 0$ with $g_1 = 0.9g_s$ (a) or $g_2 = 0$ (b), at $\epsilon = 0$ with $g_1 = 0.9g_s$ (c) or $g_1 = 1.2g_s$ (d), at $g_1 = 0.7g_s$ (e) with $g_2 = 0.6g_t$ (green, upper) or $g_2 = 0.65g_t$ (red, lower), at $\epsilon = 1g_t$ (f) with $g_2 = -0.02g_t$ (green, upper) or $g_2 = 0.02g_t$ (red, lower), given a frequency $\omega = 0.001\Omega$.

point for change of symmetry-breaking patterns (though, by a perspective view in Sec. VII, this pattern critical point may be shifted when both the bias and the nonlinear interaction are present). The regimes below and above the critical point respond to the symmetry breaking with completely different sensitivities. On the other hand, within a same linear-coupling regime, the processes of symmetry breaking may be essentially different in the presence of the bias and nonlinear interaction.

Figure 3 illustrates the different patterns of symmetry breaking in response to the bias and the nonlinear interaction, as calculated from exact diagonalization. Figure 3(a) shows the evolution of the spin expectation $\langle\sigma_z\rangle$ with respect to the variation of the bias ϵ, below g_s of linear coupling and in the absence of the nonlinear interaction g_2. We see that the amplitude of $\langle\sigma_z\rangle$ increases gradually with the bias strength, which is paramagnetic-like. Figure 3(c) shows the dependence of $\langle\sigma_z\rangle$ on the strength of the nonlinear interaction below g_s. We see that $\langle\sigma_z\rangle$ has no response to the nonlinear interaction g_2 and remains vanishing until the strength of g_2 reaches some critical point g_{2c}. Once g_2 goes beyond g_{2c}, the spin expectation $\langle\sigma_z\rangle$ jumps abruptly to a finite value and then starts approaching to saturation. This pattern with a threshold for polarization is antiferromagnetic-like. We see the essentially different patterns of symmetry breaking: there is a first-order phase transition induced by the nonlinear interaction, while there is no transition in introducing the bias. Above the critical
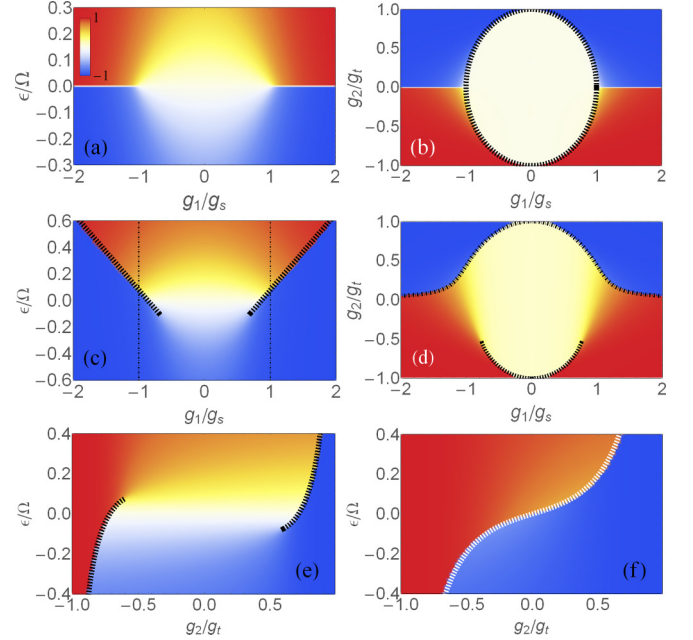
FIG. 4. Phase diagrams and analytic phase boundaries in low-frequency limit. Spin expectation $\langle\sigma_z\rangle$ at a fixed parameter (a) $g_2 = 0$, (b) $\epsilon = 0$, (c) $g_2 = 0.5g_t$, (d) $\epsilon = 10g_t$, (e) $g_1 = 0.7g_s$, (f) $g_1 = 1.2g_s$. Here $\omega = 0.01\Omega$. All panels share the same color legend for $\langle\sigma_z\rangle$ as (a). The dashed or dot-dashed curves are analytic boundaries Eqs. (16) and (17), the vertical lines in (c) are marking g_s as a reference for the boundary moving.

point g_s of the linear coupling, both the bias and the nonlinear interaction bring another pattern. In Figs. 3(b) and 3(d), we see that a tiny strength of either the bias or the nonlinear coupling will lead to dramatic change in $\langle\sigma_z\rangle$ which jumps to a finite value. This is the pattern of spontaneous symmetry breaking. This means the system is extremely sensitive to the perturbation of the bias or the nonlinear interaction, in a sharp contrast to both the paramagnetic-like pattern and antiferromagnetic-like pattern. Furthermore, as in Fig. 3(e), the interplay of the bias and the nonlinear interaction may lead to a paramagnetic-like pattern followed by a second-order-like transition (green upper line) or first-order transition (red lower line). It is also interesting to see that in the interplay with both the bias and the nonlinear interaction increasing g_1 could bring about an antiferromagnetic-like pattern but with the aforementioned first-order transition replaced by a second-order transition, as illustrated by the green (upper) line in Fig. 3(f). This occurs for the opposite signs of the bias and the nonlinear interaction. When the signs are the same another pattern could emerge, i.e., antiferromagnetic-like pattern plus successive transitions of second-order and first-order types, as shown by the red (lower) line in Fig. 3(f).

VII. PHASE DIAGRAMS AND ANALYTIC TRANSITION BOUNDARIES IN THE LOW-FREQUENCY LIMIT

To get a perspective view we plot the phase diagrams in the full parameter spaces, as in Fig. 4. Figure 4(a) shows the dependence of $\langle\sigma_z\rangle$ on the bias and the linear coupling, in the absence of the nonlinear interaction. The spin expectation $\langle\sigma_z\rangle$

has a positive value in the red (upper) region for $\epsilon > 0$ and a negative value in the blue (lower) region for $\epsilon < 0$. The white line at $\epsilon = 0$, with vanishing $\langle \sigma_z \rangle$, is parity-symmetry line from the conventional QRM. As we see, for the weak linear coupling regime $|g_1| < |g_s|$, when the bias is getting stronger, the color gradually turns from white to red (dark gray) or blue (light gray), which indicates no phase transition. Differently, for the whole strong coupling regime $|g_1| > |g_s|$, there is a sharp color change across the parity-symmetry line, indicating the spontaneous symmetry breaking. Figure 4(b) shows the behavior of $\langle \sigma_z \rangle$ in the interplay of the nonlinear interaction and the linear coupling in the absence of the bias. We see that, besides the parity-symmetry white line at $g_2 = 0$, another white round region is opened where the parity symmetry for the ground state is also unbroken. The antiferromagnetic-like pattern occurs in the regime of the round region. The dashed line along the circumference of the round region in Fig. 4(b) is the analytic boundary

$$|g_{1c}| = g_s \sqrt{1 - \widetilde{g}_2^2 / g_t^2}, \tag{15}$$

where $\widetilde{g}_2 = (1 + \chi)g_2$, which reproduces the numerical boundary.

Figures 4(c) and 4(d) illustrate the mutual influence of the bias and the nonlinear interaction over their phase diagrams. Figure 4(c) is plotted as function of bias and linear coupling, in the presence of a finite nonlinear interaction $g_2 = 0.5g_t$. Here $g_t = \omega/2$, as defined in Eq. (3), is the physical limit for the nonlinear interaction, beyond the limit the system energy becomes negatively unbound thus being unphysical. We see that, in the presence of a finite nonlinear interaction, the first order phase transition line for $\langle \sigma_z \rangle$ gets tilted from the horizontal line in zero-g_2 case. Furthermore, the transition boundary enters the regime $[-g_s, g_s]$ where originally there is no transition in the absence of the nonlinear interaction. Figure 4(d) is plotted in the g_1/g_2 plane in the presence of a finite strength of the bias $\epsilon = 0.1\Omega$. We see for $g_2 > 0$ the connection of the circle and the horizontal line originally in $\epsilon = 0$ case [Fig. 4(b)] now becomes round, with the boundary changing from a dome shape to be a hill shape. In this reshaping the transition at the boundary remains to be first order. For $g_2 < 0$, some section of the first-order round boundary disappears, with the jump of $\langle \sigma_z \rangle$ closed and softened, turning the original half-circle boundary to be an arc shape. Let us label by g_2^E the critical nonlinear interaction for the ends of the arc boundary. The analytic expression of g_2^E will be given in Eq. (33) and the dependence on the bias strength plotted in Fig. 16(b) in Sec. XIII A. Meanwhile, the arc spanning angle gets narrower than the half circle, i.e., $|g_{1c}|$ is smaller at the same value of g_2. The rest first-order arc boundary, remaining in the large-g_2-amplitude regime, shrinks with an enhanced bias.

Figures 4(e) and 4(f) show the phase diagrams at fixed linear couplings below g_s [Fig. 4(e)] and above g_s [Fig. 4(f)]. Below g_s there are two first-order boundaries in the variations of the bias and the nonlinear interaction, which are separated. When the linear coupling gets stronger the two boundaries are curved, with their ends getting closer and finally connected to form one first-order boundary above g_s.

For a quantitative description, we extract the analytic boundary marked by g_{1c} or ϵ_c as follows:

$$|g_{1c}| = g_s \left[1 + \frac{g_t \epsilon}{\widetilde{g}_2 \Omega} \right] \sqrt{1 - \widetilde{g}_2^2 / g_t^2}, \tag{16}$$

$$\epsilon_c = \frac{\widetilde{g}_2}{g_t} \left[\frac{|g_1|/g_s}{\sqrt{1 - \widetilde{g}_2^2/g_t^2}} - 1 \right] \Omega. \tag{17}$$

We leave the analytic derivation in Sec. XIII A. Note here, whereas for $g_2 \epsilon > 0$ the extension of boundary is unlimited, for $g_2 \epsilon < 0$ the validity regime is $|g_2| < g_2^E$ which is the arc boundary. We leave the detail of derivation in Sec. XIII. Setting $\epsilon = 0$ retrieves the round boundary $|g_{1c}| = g_s \sqrt{1 - \widetilde{g}_2^2 / g_t^2}$ in the absence of bias [24]. We plot the analytic boundaries by the dashed or dot-dashed lines in Figs. 4(b)–4(f), which are in good agreements with the numerical boundaries.

VIII. TRICRITICALITY-(I) IN THE LOW-FREQUENCY LIMIT

In Fig. 4(b) one may notice on each side $g_1 = \pm g_s$ is a triple point where the round boundary and horizontal line are crossing. Unlike the conventional tricritical point where a second-order boundary and a first-order boundary meet, this triple point connects two first-order boundaries. Still it is particular as both the two first-order boundaries become second-order at this triple point. In the presence of the bias, this triple point will move and turn to a conventional tricritical point.

In Fig. 5(a), in the absence of the bias by the purple dot-dashed line ($\epsilon/g_t = 0$) we show the spin expectation discontinuity $\Delta \sigma_z$, i.e., the jump of $\langle \sigma_z \rangle$ across the boundary, with the finite value of $\Delta \sigma_z$ representing the first-order transition. The transition becomes second-order at g_s as indicated by the vanishing of $\Delta \sigma_z$. In the presence of the bias, this second-order transition also turns to be first order, as we illustrate by $\epsilon/\Omega = 0.001$, 0.01, and 0.04 in the low-frequency limit ($\epsilon/g_t = 1$, 10, and 40 if taking $\omega = 0.001\Omega$). With the bias increasing, the shape of the $\Delta \sigma_z$ minimum evolves from a sharp dip into a round valley. Figure 5(b) provides a view of $\Delta \sigma_z$ in the g_2 dimension, which includes both boundaries in the positive and negative g_2 regimes. The vanishing-$\Delta \sigma_z$ point at zero bias is extending into a vanishing-$\Delta \sigma_z$ window at finite biases. In the negative g_2 regime the remaining finite-$\Delta \sigma_z$ section in Fig. 5(b) corresponds to the boundary arc. In the positive g_2 regime, it is worthwhile to follow the evolution of the minimum position of $\Delta \sigma_z$, which is moving away from the original point $g_2 = 0$. As aforementioned, this minimum point is originally a triple point in the absence of the bias, now in the presence of the bias it will turn out to be an imprint of tricriticality.

Indeed, when scanning g_1 in Fig. 5(c), as demonstrated by the case $g_2 = 0.1g_t$ [blue (right) line] we see a three-phase-like scenario: first, a flat region in spin expectation $\langle \sigma_z \rangle$; second, a fast-rising region; finally, jumping into a region with opposite sign. The three phases look more distinct in the evolution of the spin expectation in x direction, $\langle \sigma_x \rangle$, as shown by the blue (right) line in Fig. 5(d). Essential changes of the three phases may be indicated by $\langle a^+ + a \rangle$ which is
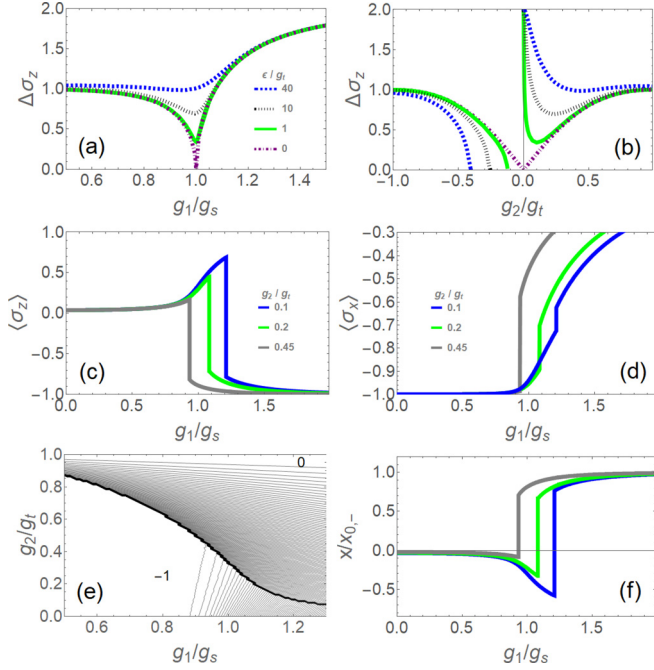
FIG. 5. Tricriticality-(i) in low-frequency limit. (a) Spin expectation discontinuity $\Delta\sigma_z$ along the transition boundary in $g_2 > 0$ regime as a function of g_1 for $\epsilon = 0g_t$ (purple dot-dashed), $1g_t$ (green solid), $10g_t$ (black dotted), and $40g_t$ (blue dashed) at $\omega = 0.001\Omega$. (b) $\Delta\sigma_z$ as a function of g_2. (c–f) Three-phase behavior of $\langle\sigma_z\rangle$ (c), $\langle\sigma_x\rangle$ (d, e), $\langle\hat{x}\rangle$ (f) for $\epsilon = 40g_t$. Panels (c, d, f) give illustrations with fixed $g_2 = 0.1g_t$ (blue, right), $g_2 = 0.2g_t$ (green, middle), and $g_2 = 0.45g_t$ (gray, left), while (e) is a contour plot.

effective spatial particle position x (we shall discuss more in Secs. XI and XII). As shown in Fig. 5(f), the effective particle resides closely around the origin in the first phase, moves obviously away from origin in the second phase and jumps abruptly to the other side in the third phase. These three phases are separated by two transition-like points, the first transition is second-order-like and the second one is of first order. When the bias strength increases, the two transitions get closer to each other and finally meet, as illustrated by $g_2 = 0.2g_t$ [green (middle) lines] and $g_2 = 0.45g_t$ [gray (right) lines] in Figs. 5(c), 5(d), and 5(f). Such a scenario of two separate transitions converging to one transition forms a tricritical-like point, which can be seen more clearly by the contour plot of $\langle\sigma_x\rangle$ in Fig. 5(e). This tricritical-like point is located around the aforementioned $\Delta\sigma_z$ minimum position.

IX. NOVEL TRICRITICALITIES AND TRIPLE POINTS AT FINITE FREQUENCIES

The low-frequency limit discussed in previous sections is also the semiclassical limit, as the wave-packet size is so small that it can be regarded as a semiclassical mass point (as discussed in Sec. III C). In such a semiclassical limit, in each quadrant of the phase diagrams in Fig. 4 the nonlinear interaction induces only one transition in the absence of the bias and at most two transitions in the interplay with the bias. However, the spontaneous symmetry breaking occurs immediately upon any tiny strength of the bias or nonlinear interaction. In this
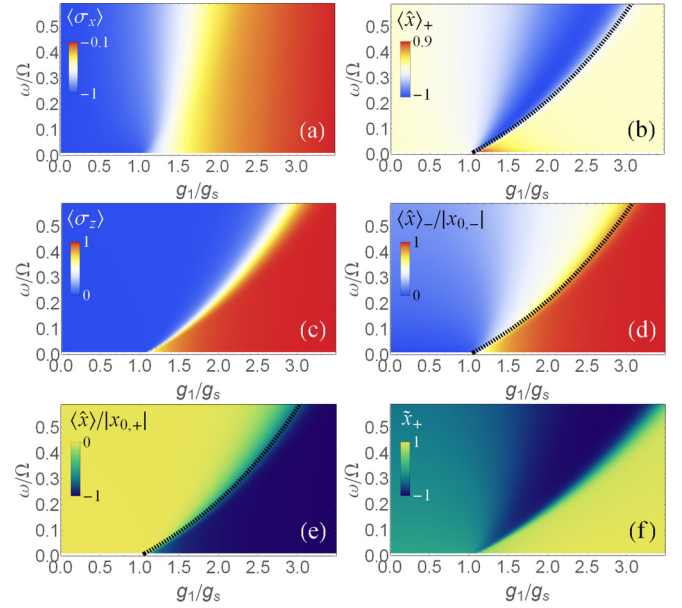
FIG. 6. Tricriticality-(ii) induced by frequency ω. Phase diagrams of different quantities by frequency variation (ω) at $\epsilon = 0.001g_t$ with $g_2 = 0$ (a,c,e) and $g_2 = 0.0001g_t$ with $\epsilon = 0$ (b, d, f) for (a) $\langle\sigma_x\rangle$, (b) $\langle\hat{x}\rangle_+$, (c) $\langle\sigma_z\rangle$, (d) $\langle\hat{x}\rangle_-/|x_{0,-}|$ ($\hat{x} = (a + a^\dagger)/\sqrt{2}$), (e) $\langle\hat{x}\rangle/|x_{0,+}|$, and (f) $\tilde{x}_+ = \langle\hat{x}\rangle_+/(|x_{0,+}|\rho_+)$. The dashed lines in panels (b–e) are g_{1c}^{II} extracted from analytic Eqs. (18) and (19).

section, we shall see that the full quantum-mechanical effect at finite frequencies will change this picture and lead to richer scenarios. We find that additional transitions appear, tricriticalities and triple points arise, and the spontaneous symmetry breaking exhibits a fine structure.

A. Additional transition and Tricriticality-(ii) induced by the frequency, respectively, in the bias or the nonlinear interaction

The tricriticality in Sec. VIII occurs in the low-frequency limit. The transitions and the tricriticality arise from the competition and interplay of the bias, the nonlinear interaction and the linear coupling. In such a situation, different physical quantities exhibit imprints of each transition at a same transition point, as one can see from Figs. 5(c), 5(d), and 5(f). Here we show another kind of tricriticality induced by the frequency which has a different nature and transition positions diverge for different physical quantities.

In Fig. 6, we show a variety of physical quantities with the dependence on the frequency ω, under a fixed bias $\epsilon = 0.1\,\Omega$ in Figs. 6(a), 6(c), and 6(e) or a fixed nonlinear interaction $g_2 = 0.01g_t$ in Figs. 6(b), 6(d), and 6(f). The two-parameter cases have similar behavior despite some detail and sign difference for some quantities. As expected, in the low-frequency limit both $\langle\sigma_x\rangle$ [Fig. 6(a)] and $\langle\sigma_z\rangle$ [Fig. 6(c)] show one transition at a same point around $g_1 = g_s$. However, when the frequency is raised, $\langle\sigma_x\rangle$ and $\langle\sigma_z\rangle$ respond differently. In fact, the transition in $\langle\sigma_x\rangle$ is not much affected by the frequency except for some softening of the transition, whereas the transition in $\langle\sigma_z\rangle$ is moving obviously toward the larger-g_1 direction. The diverging evolutions of the transition positions of $\langle\sigma_x\rangle$ and $\langle\sigma_z\rangle$ indicate an additional transition induced by the finite

frequency, thus the one transition in the low-frequency limit becomes two transitions at finite frequencies. It also seems peculiar that the spin expectations $\langle \sigma_x \rangle$ and $\langle \sigma_z \rangle$ respond to the two transitions, respectively: the first transition induces response in $\langle \sigma_x \rangle$ but leaves no imprints in $\langle \sigma_z \rangle$, while the second transition shows a strong onset signal in $\langle \sigma_z \rangle$ but gives no sign in $\langle \sigma_x \rangle$. This additional transition can also be seen from the effective particle position or displacement $\langle \widehat{x} \rangle = \langle a^\dagger + a \rangle / \sqrt{2}$, as shown in Fig. 6(e).

The two diverging transitions can be also detected simultaneously by a single physical quantity, such as the spin-filtered displacement $\langle \widehat{x} \rangle_\pm = \langle a^\dagger + a \rangle_\pm / \sqrt{2}$ which only counts the contribution from one spin component, as shown in Figs. 6(b) and 6(d), where it is quite clear to visualize two boundaries corresponding to the two transitions. To have unified upper and lower bounds for plotting we also introduce the normalized spin-filtered displacement $\widetilde{x}_\pm = \langle a^\dagger + a \rangle_\pm / (\sqrt{2} \rho_\pm |x_{0,\text{sign}(-\widetilde{g}_2)}|)$, where $\rho_\pm = \langle \psi^\pm | \psi^\pm \rangle = (1 \pm \langle \sigma_z \rangle)/2$ is the spin-component weight and $x_{0,\pm}$ is the potential displacement [as defined in Eq. (8)]. Besides the normalization, $\widetilde{x}_\pm$ provides another convenience that it has three regimes of values, respectively, for the three phases separated by the two transitions. Thus, the three phases can can be distinguished by three colors, as shown in Fig. 6(f). It should be mentioned that at higher frequencies there is some discrepancy for the second transition point from $\widetilde{x}_\pm$. This spurious transition discrepancy is simply coming from the cancellation effect around the transition from its numerator $\langle a^\dagger + a \rangle_\pm$ and denominator $\rho_\pm$, while separately both $\langle a^\dagger + a \rangle_\pm$ and $\rho_\pm$ have the right second transition point. Nevertheless, the discrepancy at low frequencies is negligible so we can still use it for further discussions by the advantages of its normalization and value(color)-phase correspondence.

Reversely in lowering the frequency, the two boundaries of the three phases will converge to one point, thus forming a triple point and another kind of tricriticality. In a conventional tricriticality each two adjacent phases adjoin through a boundary, here among the three phases there are two adjacent phases connected by one critical point at zero frequency. It should be noted that the tricriticality of this case, as labeled by (ii), is distinguished from Tricriticality-(i) in Sec. VIII. Tricriticality-(i) happens in the presence of both the bias and the nonlinear interaction, while Tricriticality-(ii) here occurs in the respective presence of the bias or the nonlinear interaction. From the mechanism clarification in Sec. XII we will see that the additional transition and tricriticality originate from a full-quantum-mechanical effect, in a contrast to the semiclassical effect in the low-frequency limit.

B. Tricriticality-(iii) induced by the bias or the nonlinear interaction at finite frequencies

It will provide another view by fixing a finite frequency and varying the bias or the nonlinear interaction. As described in Sec. VII, in the low-frequency limit we see from Figs. 4(a) and 4(b) that in each quadrant of the phase diagrams there is no more than one transition. As revealed in Sec. IX A, at a finite frequency the single transition turns to be two successive transitions. The variation of the bias or the nonlinear interaction
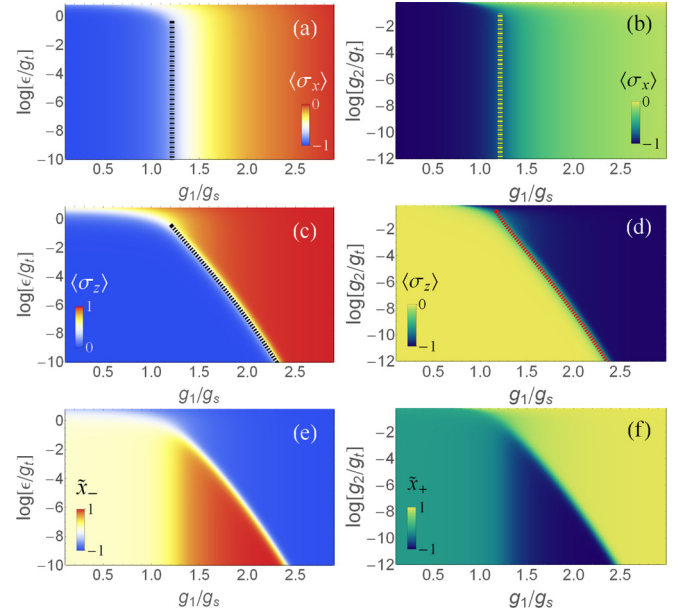
FIG. 7. Tricriticality-(iii) induced by the bias or the nonlinear interaction at a finite frequency. Phase diagrams at $\omega = 0.1\Omega$ for variation of ϵ at $g_2 = 0$: (a) $\langle \sigma_x \rangle$, (c) $\langle \sigma_z \rangle$, (e) $\widetilde{x}_-$. Phase diagrams for variation of g_2 at $\epsilon = 0$: (b) $\langle \sigma_x \rangle$, (d) $\langle \sigma_z \rangle$, (f) $\widetilde{x}_+$. The dot-dashed lines in panels (a, b) are analytic g_{1c}^{I} and the dashed lines in panels (c, d) are analytic ϵ_c^{II} and g_{2c}^{II} in Eqs. (18) and (19). The base of the logarithm is 10 throughout the paper.

will influence the transitions and induce a third tricriticality which we label by Tricriticality-(iii).

The successive transitions can be seen more clearly from a zoom-in view by a logarithm scale for the variations of ϵ and g_2, as illustrated by Fig. 7 at a finite frequency $\omega = 0.1\Omega$. Figures 7(a), 7(c), and 7(e) present the phase diagrams for the pure bias dependence without the nonlinear interaction and Figs. 7(b), 7(d), and 7(f) for the nonlinear interaction in the absence of the bias. To distinguish the two transitions we label the transition in $\langle \sigma_x \rangle$ by g_{1c}^{I} and that in $\langle \sigma_z \rangle$ by g_{1c}^{II}. We see in Figs. 7(a) and 7(b) that the first transition (second-order-like) in $\langle \sigma_x \rangle$ does not vary at weak strengths of ϵ or g_2, except that the transition point at low frequencies shifts a bit from $g_{1c} \sim g_s$ to $g_{1c}^{\text{I}} \approx \sqrt{\omega^2 + \sqrt{\omega^4 + g_s^4}}$ [20] due to the width of wave packet in the wave-packet splitting. In a sharp contrast, the second transition is very sensitive to the variation of the bias and the nonlinear interaction. In fact, as demonstrated by Figs. 7(c) and 7(d), the transition point g_{1c}^{II} has a logarithmic dependence on ϵ and g_2. Analytically we find the second boundary as a function of g_1 (see the derivation in Sec. XIII):

$$|\epsilon_c^{\text{II}}| = \frac{(1-t)\Omega}{4\delta_c \zeta} \exp\left[-\frac{\zeta^2 \overline{g}_1^2 \Omega}{2\omega} \right], \quad \text{for } g_2 = 0, \quad (18)$$

$$|\widetilde{g}_{2c}^{\text{II}}| = \frac{(1-t)g_t}{\delta_c \zeta^3 \overline{g}_1^2} \exp\left[-\frac{\zeta^2 \overline{g}_1^2 \Omega}{2\omega} \right], \quad \text{for } \epsilon = 0, \quad (19)$$

where $\overline{g}_1 \equiv g_1/g_s$, $\delta_c = e^{-1}$, $t = (1-\zeta)^2/2 + \omega/(\overline{g}_1^2 \Omega)$ and $\zeta = (1 - \overline{g}_1^{-4})^{1/2}$. The analytic boundaries $\epsilon_{2c}^{\text{II}}$ and g_{2c}^{II} are plotted as the dashed lines in Figs. 7(c) and 7(d), in good agreements with the numerical results.

With the strength increase of the bias or the nonlinear interaction, the two transitions, respectively, reflected in $\langle\sigma_x\rangle$ and $\langle\sigma_z\rangle$ are getting closer and finally meet to form Tricriticality-(iii). A better view of this tricriticality can be obtained from $\widetilde{x}_\pm$ as in Figs. 7(e) and 7(f) where three phases are distinctly represented by three colors (value regimes). Above the tricritical point it is one transition of first-order type, while below the tricritical point the transition is bifurcated into a second-order-like transition and a first-order-like one. Exactly speaking, in the bias case the transition above the tricritical point is a short extension from the first-order transition below the tricritical point. This transition soon gets softened and fades away when the linear coupling g_1 is reduced to below g_s. In the nonlinear interaction case, the first-order-like transition covers the entire g_2 regime thus also the whole g_1 regime.

To distinguish Tricriticality-(iii) from Tricritcalities (i) and (ii) let us mention the differences. Tricritcality-(i) in the low-frequency limit revealed in Sec. VIII occurs in the presence of both the bias and the nonlinear interaction. Tricriticality-(iii) here needs only the bias or the nonlinear interaction. Tricriticality-(ii) unveiled in Sec. IX A is induced by the variation of the frequency, here Tricriticality-(iii) is induced by the bias or nonlinear interaction at a fixed finite frequency.

The scenario of Tricriticality-(iii) also gives rise to a fine structure of the spontaneous symmetry breaking for the finite frequency case. Note that the negative-$\epsilon(g_2)$ regime has the same tricritical scenario as the positive-$\epsilon(g_2)$ regime, except for being antisymmetric for $\langle\sigma_z\rangle$ and symmetric for $\langle\sigma_z\rangle$ in the quadrants of the phase diagrams. Thus, rather than an immediate jump of $\langle\sigma_x\rangle$ from zero to a finite value upon the opening of the bias or the nonlinear interaction, there is now a window within which the parity symmetry of the ground state is maintained to some large extent, as indicated by the vanishing $\langle\sigma_z\rangle$. Out of the window the symmetry is broken. This window becomes narrower when the linear coupling gets stronger, but can be widened by a higher frequency.

C. Sensitivity competition of the bias and the nonlinear interaction in spontaneous symmetry breaking

The spontaneous symmetry breaking means that the symmetry is vulnerable to the perturbation of the bias or the nonlinear interaction. It may be worthwhile to compare the symmetry-breaking sensitivity to the bias and the nonlinear interaction. As described in the paramagnetic-like and antiferromagnetic-like symmetry patterns in Secs. VI and VII, let us remind that in the weak linear coupling regime $g_1 < g_s$ the polarization $\langle\sigma_z\rangle$ is more sensitive to the bias but responseless to the nonlinear interaction within a threshold g_{2c}. We find this sensitivity tendency is reversed in the strong linear coupling regime $g_1 > g_s$. It turns out that in this regime the symmetry breaking finds a higher sensitivity to the nonlinear interaction than the bias. In Fig. 8(a), we demonstrate that the symmetry breaking occurs earlier in the nonlinear interaction (orange dashed line, $\epsilon = 0$) in the sense that the bias needs to have a relatively stronger strength (blue dot-dashed line, $g_2 = 0$) to bring about the transition. Figure 8(b) shows the ratio of the critical-like strengths between the bias and the nonlinear interaction. One sees the critical strength of the
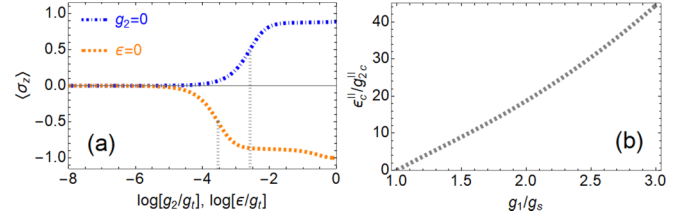
FIG. 8. Sensitivity competition for spontaneous symmetry breaking. (a) $\langle\sigma_z\rangle$ depending on ϵ at $g_2 = 0$ (orange dashed) and on g_2 at $\epsilon = 0$ (blue dot-dashed) at $g_1 = 1.5g_s$ and $\omega = 0.1\Omega$. (b) Threshold ratio $\epsilon_c^{\mathrm{II}}/g_{2c}^{\mathrm{II}}$ depending on g_1. The base of the logarithm is 10 throughout the paper.

bias is one or two orders larger than the nonlinear interaction. Moreover, this ratio is growing with the linear coupling g_1.

One can see more clearly from the analytic boundary Eqs. (18) and (19). We obtain the ratio between the critical bias and nonlinear interaction

$$\frac{\left|\epsilon_c^{\mathrm{II}}\right|}{\left|\widetilde{g}_{2c}^{\mathrm{II}}\right|} = \frac{\zeta^2 \overline{g}_1^2 \Omega}{4 g_{\mathrm{t}}}. \tag{20}$$

On the one hand, the low-frequency contributes to the order difference as $g_{\mathrm{t}} = \omega/2$. On the other hand, the ratio is proportional to $\overline{g}_1^2$ which grows parabolically with the strength of the linear coupling. In addition, ζ [defined below Eq. (19)] starts for a small value at $g_1 = g_s$ and soon approaches to the value 1 in the increase of g_1, which also contributes to the ratio growing at the beginning. Thus, unlike in the regime below g_s, the parity symmetry in the regime beyond g_s is more sensitively broken by the perturbation of nonlinear interaction than that of the bias, unless nearby g_s. This sensitivity priority of the nonlinear interaction comes from the entanglement of the nonlinear interaction and the linear coupling, as indicated by Eq. (9) in Sec. XII.

D. Tricriticality plus another triple point (iv) induced by the interplay of the bias and the nonlinear interaction at finite frequencies

In Tricriticality-(iii) we have considered the bias and the nonlinear interaction, respectively. Now we should address how the transitions and the fine structure of spontaneous symmetry breaking are affected by the interplay of the bias and nonlinear interaction. We illustrate in Figs. 9(a)–9(d) the phase diagrams by variation of the bias in the presence of a fixed nonlinear interaction, and in Figs. 9(e)–9(h) the phase diagrams by variation of the nonlinear interaction in the presence of a fixed bias. As one can see, besides the transition boundaries I and II, two more boundaries appear as we mark by III and IV. As expected, the onset of transition I can be seen by the start of increasing in $\langle\sigma_x\rangle$, as shown in Figs. 9(a) and 9(e). Transitions II, III, and IV can be clearly observed in $\langle\sigma_z\rangle$ as demonstrated in Figs. 9(b) and 9(f).

Although transition I is missed by $\langle\sigma_z\rangle$, all the transitions I–IV leave some imprints in $\widetilde{x}_\pm$ as in Figs. 9(c), 9(d) and 9(g). The boundaries can also be all visualized by the peaks of the susceptibility $d\widetilde{x}_\pm/dg_1$, as illustrated in Fig. 9(h). For a fixed nonlinear interaction in Figs. 9(b)–9(d), the boundary IV is tilted upwards, with the critical bias increasing with the linear coupling. For a fixed bias in Figs. 9(f)–9(h), the boundary
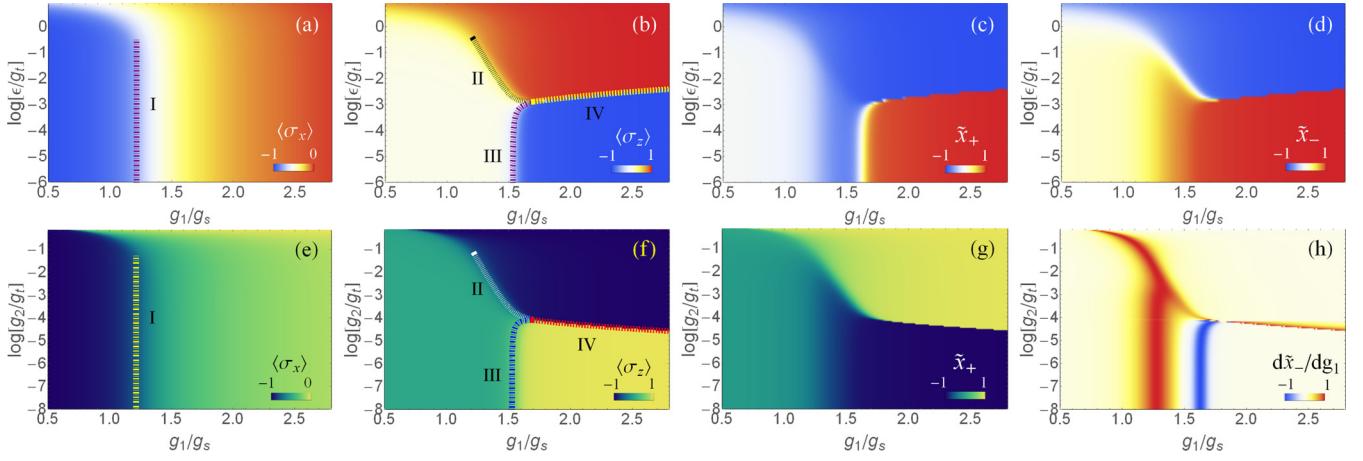
FIG. 9. Tricriticality plus another triple point (iv) in the interplay of the bias the nonlinear interaction. Phase diagrams at $\omega = 0.1\Omega$ for variation of ϵ at $g_2 = 10^{-4}g_t$: (a) $\langle\sigma_x\rangle$, (b) $\langle\sigma_z\rangle$, (c) $\tilde{x}_+$, (d) $\tilde{x}_-$. Density plot for variation of g_2 at $\epsilon = 10^{-3}g_t$: (e) $\langle\sigma_x\rangle$, (f) $\langle\sigma_z\rangle$, (g) $\tilde{x}_+$, (h) $d\tilde{x}_-/dg_1$ scaled by the local peak amplitude. The lines are our analytic g_{1c}^I in panels (a, e), ϵ_c^{II}, ϵ_c^{III}, ϵ_c^{IV} in panel (b), and g_{2c}^{II} g_{2c}^{III}, g_{2c}^{IV} in panel (f) [see Eqs. (21)–(26)]. The base of the logarithm is 10 throughout the paper.

IV is tilted downwards, with the critical nonlinear interaction decreasing with the linear coupling.

In Fig. 9 the crossing of the boundaries I and II forms a first triple point around $g_1 = 1.2g_s$, which actually is tricriticality-(iii) in the presence of only the bias or the nonlinear interaction. Now in the presence of both the bias and the nonlinear interaction, with the enhancement of the linear coupling the boundaries II and III get closer to the tilted boundary IV and seem to form a second triple point around $g_1 = 1.6g_s$. We label such a situation with coexisting tricriticality and another triple point by (iv).

We extract in the leading order the analytic boundaries expressed by the bias as a function of the linear coupling and the nonlinear interaction

$$\epsilon_c^{II} = \frac{(1-t)\Omega}{4\delta_c\zeta}\exp\left[-\frac{\zeta^2\overline{g}_1^2\Omega}{2\omega}\right] + \frac{1}{4}\zeta^2\overline{g}_1^2\overline{g}_2\Omega, \quad (21)$$

$$\epsilon_c^{III} = -\frac{(1-t)\Omega}{4\delta_c\zeta}\exp\left[-\frac{\zeta^2\overline{g}_1^2\Omega}{2\omega}\right] + \frac{1}{4}\zeta^2\overline{g}_1^2\overline{g}_2\Omega, \quad (22)$$

$$\epsilon_c^{IV} = \frac{1}{4}\zeta^2\overline{g}_1^2\overline{g}_2\Omega, \quad (23)$$

or tracked by the nonlinear interaction in variations of the linear coupling and the bias

$$\tilde{g}_{2c}^{II} = \frac{(1-t)g_t}{\delta_c\zeta^3\overline{g}_1^2}\exp\left[-\frac{\zeta^2\overline{g}_1^2\Omega}{2\omega}\right] + \frac{4\epsilon}{\zeta^2\overline{g}_1^2\Omega}g_t, \quad (24)$$

$$\tilde{g}_{2c}^{III} = -\frac{(1-t)g_t}{\delta_c\zeta^3\overline{g}_1^2}\exp\left[-\frac{\zeta^2\overline{g}_1^2\Omega}{2\omega}\right] + \frac{4\epsilon}{\zeta^2\overline{g}_1^2\Omega}g_t, \quad (25)$$

$$\tilde{g}_{2c}^{IV} = \frac{4\epsilon}{\zeta^2\overline{g}_1^2\Omega}g_t, \quad (26)$$

where $\overline{g}_2 = \tilde{g}_2/g_t$. As shown in Figs. 9(b) and 9(f) the analytic boundaries match the numerical ones fairly well. We see that the interplay of the bias and the nonlinear interaction contributes to the second term of the boundaries II and III, as an additional term to Eqs. (18) and (19). Exactly speaking, since the second term is equal to ϵ_c^{IV} or $\tilde{g}_{2c}^{IV}$, the mathematical triple point (iv) is at the infinity of linear coupling. However, in real-

ity, although boundary IV is actually composed of boundaries II and III with $\tilde{g}_{2c}^{IV}$ or ϵ_c^{IV} as their center, they are too close to be distinguished when the boundaries are tilted in the regime of the strong linear coupling. Thus, effectively triple point (iv) appears at a finite value of the linear coupling.

E. Tricriticality plus another triple point (v) induced by frequency in the interplay of the bias and the nonlinear interaction

Now let us come back to the frequency dimension. In Sec. IX A, we have seen that the frequency induces a tricritical point in the respective presence of the bias or the nonlinear interaction. Now we consider frequency effect in the presence of both the bias and the nonlinear interaction. Imagine we are standing at the boundary IV in Fig. 9, Eqs. (21)–(26) indicate that increasing the frequency would open the gap between the boundary IV and the boundaries II, III, thus inducing another triple-like point. We show such a scenario by Fig. 10 in the g_1-ω plane. As one can see, apart from the first frequency-induced tricritical point [tricriticality-(ii) as
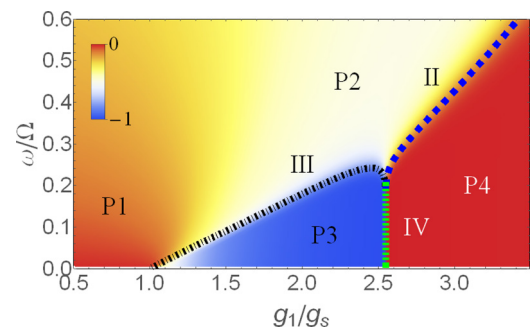
FIG. 10. Tricriticality plus another triple point (v) induced by frequency variation. Phase diagram of $\langle\hat{x}\rangle_+/|x_{0,+}|$ in g_1-ω plane at $\epsilon = 0.5 \times 10^{-4}\Omega$ and $\log[g_2/g_t] = -4.5$. P1, P2, P3, and P4 mark the different phases. The blue long-dashed, black dot-dashed, and green dashed lines are analytic boundaries II, III, and IV, respectively.

aforelabeled] around $g_1 = 1.0g_s$, another triple point appears around $g_1 = 2.5g_s$ which is the location of g_{1c}^{IV} at a fixed bias $\epsilon = 0.0001\Omega$ and a nonlinear interaction $\log[g_2/g_t] = -4.5$. More generally, from Eq. (26) we extract the location of the second frequency-induced triple point as

$$g_{1c}^{IV} = g_s \sqrt{\frac{2\epsilon + \sqrt{4\epsilon^2 + \overline{g}_2^2 \Omega^2}}{\Omega \overline{g}_2}}. \qquad (27)$$

We label this situation with coexisting tricriticality and another triple point by (v). Exactly speaking, this triple point is mathematically located at $\omega = 0$, but effectively the triple point seems to form at some finite frequency as boundaries II and III are already too close to be distinguished at the finite frequency.

F. Tendency for four successive transitions

From the discussions in Sec. VIII, we know that in the low-frequency limit there are at most two transitions in increasing g_1. The various situations for the occurrence of tricriticality described above in Secs. IX D and IX E demonstrate that finite frequencies can lead to three transitions. Still, it might be possible to go even further. A closer look at Fig. 10, we can see the boundaries II and III forms a dip shape around $g_1 = 2.5g_s$. The boundary III is actually a nonmonotonic function of g_1. Around $\omega = 0.22\Omega$, in fact increasing g_1 goes across the boundary III twice. Let us mark the different phases by P1, P2, P3, P4. In increasing g_1 one starts with phase P1. After the first second-order transition the system enters phase P2. Then the first time across boundary III brings the system from phase P2 to phase P3. By the second time across boundary III the system re-enters Phase P2. After the short re-entrance of phase P2, the system transits to phase P4 through boundary II. Thus, in this regime the system actually experiences four successive transitions, i.e., transitions I, III, III, and II, going through phases P1, P2, P3, P2, P4. This tendency of the second additional transition indicates that finite frequencies induces a subtle energy competition beyond the semiclassical picture.

X. QUADRUPLE POINTS AND TETRACRITICALITY

In last section we have seen that at finite frequencies the system can have four phases P1, P2, P3, and P4 with three, even four transitions. We have addressed a variety of situations in which tricriticality may occur. Since we have four phases totally, one may wonder whether it is possible for all the four phases to meet and form a quadruple point and tetracriticality. We find this can happen indeed. The possibility is indicated from the last transition point Eq. (27) which, if the bias ϵ is being reduced, approaches to the first transition $g_{1c}^I = g_s$ in the low-frequency limit. This process of transition converging is shown in Fig. 11, where we set $\epsilon = 0.0005g_t$ which is proportional to the frequency. As one sees, all three transitions boundaries finally collapses to one point around $g_1 = g_s$, thus forming a quadruple point and a kind of tetracriticality. Again here, the direct connection boundary for phases P1 and P4 is a critical point at zero frequency rather than a boundary line as in conventional case.
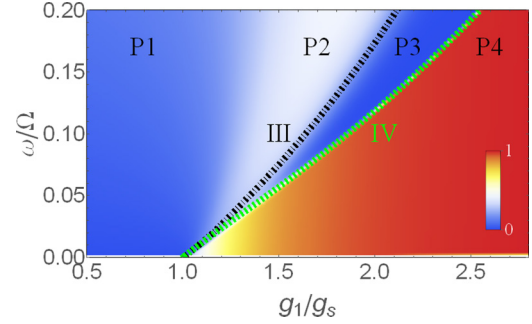
FIG. 11. Quadruple point and tetracriticality. Phase diagram of $\langle \hat{x}_- \rangle / |x_{0,-}|$ in g_1-ω plane at $\log[g_2/g_t] = -4.5$ with $\epsilon = 0.0005g_t$. In low-frequency limit the four phases P1, P2, P3, and P4 meet around $g_1 = g_s$, forming a quadruple point and a tetracriticality.

The quadruple point is illustrated for a small value of g_2. One would also get similar quadruple points in other values of g_2. The track by varying g_2 continuously would yield a section of quadruple line along $|g_1| = g_s \sqrt{1 - \widetilde{g}_2^2/g_t^2}$ which is actually the transition boundary Eq. (15) in the absence of the bias. Since the quadruple line is parabolic in small values of $\widetilde{g}_2$, in weak nonlinear interactions the quadruple points turn out to be around $|g_1| = g_s$ in the leading order, as we have seen in the illustrated Fig. 11.

XI. CHANGEOVERS OF THE WAVE FUNCTION IN THE PHASE TRANSITIONS

To see the essential changes of quantum state in the transitions we shall monitor the evolution of the wave function. In Fig. 12 we show the spin-up and spin-down components of the wave function that goes through successive transitions in the variation of the linear coupling, under fixed values of bias and nonlinear interaction. Figures 12(a) and 12(b) are in the low-frequency limit, while Figs. 12(c)–12(f) are finite-frequency cases. Note different choices of frequency will change g_t which is taken to be the strength reference of the nonlinear interaction as well as the bias. Nevertheless by fixing two ratios $\widetilde{g}_2/g_t$ and ϵ/Ω we have the same transition point of the last transition IV, around $g_1 \sim 2.5g_s$, which is the common one in the different frequency illustrations, as indicated by Eq. (27).

In the low-frequency limit (illustrated by $\omega = 0.001\Omega$) the wave packet is very thin, just like a mass point of an effective particle, as one sees from Figs. 12(a) and 12(b). Starting from $g_1 = 0$ till the first transition $g_1 \sim 1.0g_s$ the effective particle always stays at the origin $x = 0$. Beyond the first transition it starts to go away from the origin, and shifts to the other side at the next transition around $g_1 \sim 2.5g_s$.

At a finite frequency $\omega = 0.1\Omega$ in Figs. 12(c) and 12(d) the wave packet is obviously broadened, but still remaining in a *single-branch* structure and staying around the origin before the first transition. After the first transition the wave packet splits into two branches in both the spin components, which is different from the low-frequency limit. Strengthening more the linear coupling g_1 triggers the second transition around $g_1 \sim 1.6g_s$ where one branch of the wave packet is broken. In such a *broken-branch* state the wave packet on one side
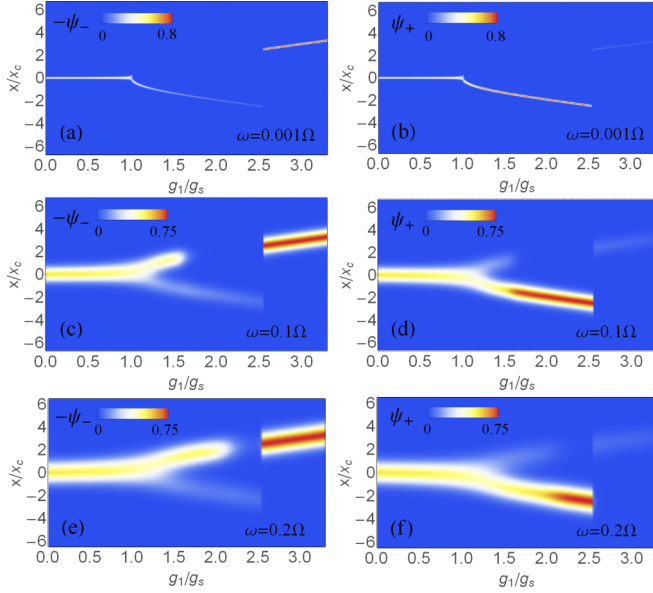
FIG. 12. Variations of the wave function components $-\psi_-(x)$ (a, c, e) and $\psi_+(x)$ (b, d, f) in phase transitions. The minus sign is added for $\psi_-(x)$ to have the same color reference of zero value as $\psi_+(x)$. (a, b) $\omega = 0.001\Omega$, $\epsilon = 0.1g_t$. (c, d) $\omega = 0.1\Omega$, $\epsilon = 0.001g_t$. (e, f) $\omega = 0.2\Omega$, $\epsilon = 0.0005g_t$. Here we fix $\log[g_2/g_t] = -4.5$ and the effective spatial position is scaled by $x_c = \sqrt{2}g_s/\omega$.

FIG. 13. Semiclassical mechanisms for the different patterns of symmetry breaking. The potentials $v_\pm(x)$ in spin-up [blue (dark gray)] and spin-down [orange (light gray)] components for (a–c) $\epsilon = 0$, $g_2 = 0$, (d–f) $\epsilon \neq 0$, $g_2 = 0$, and (g–i) $g_2 \neq 0$, $\epsilon = 0$. The linear coupling regimes are (a, d, g) $g_1 = 0$, (b, e, h) $g_1 < g_s$, and (c, f, i) $g_1 > g_s$. The dots mark the effective semiclassical particle positions in the spin-up and spin-down potentials.

vanishes in both spin components and all the weight goes to the branch on the other side. Further increase of g_1 induces the third transition, around $g_1 \sim 2.5g_s$, which switches the broken-branch state from one one side to the other side. These three successive transitions correspond to the boundaries I, III, and IV in Figs. 9(e) and 9(f) and Fig. 10. Besides the different feature of the two-branch structure after the first transition, the second transition is additional relative to the low-frequency limit. At a higher frequency $\omega = 0.2\Omega$ in Figs. 9(e) and 9(f) the second transition point moves to a stronger linear coupling around $g_1 \sim 2.2g_s$. We also see that in the first transition the splitting of the wave packet is continuous, which corresponds to the second-order transition in $\langle \sigma_x \rangle$. The changeover of the wave-function structure is discontinuous-like in the second and third transitions, which matches the first-order-like transitions in $\langle \sigma_z \rangle$.

The example is illustrated at small values of bias and nonlinear interaction. It might be worth mentioning that at a fixed frequency a stronger bias or nonlinear interaction can lead to a mixed quantum state, i.e., one spin component in the two-branch state and the other spin component in the broken-branch state. Further potential imbalance from the bias or nonlinear interaction will finally drive both spin components into broken-branch states.

XII. MECHANISMS

In this section we shall clarify the mechanisms underlying the various patterns of symmetry breaking, scaling of the Stark-like term and the successive transitions in the tricriticalities and the tetracriticality. We will also explain why

the quantities, $\langle \sigma_z \rangle$, $\langle \sigma_x \rangle$, $\langle \hat{x} \rangle$, and $\langle \hat{x} \rangle_\sigma$, respond differently to the transitions.

A. Semiclassical picture for the various patterns of symmetry breaking

The various patterns of symmetry breaking in the low-frequency limit can be readily explained in the semiclassical consideration introduced in Sec. III C. Here, rather than the variational total energy, we shall give a physical picture for the competitions of different energy parts. Since the contribution of the kinetic energy to the ground state is vanishing in the semiclassical limit, the phase transitions and the system properties are decided by the competition of the potential $v_\pm$ and the tunneling Ω. In Fig. 13, according to different patterns of symmetry breaking we plot the potentials v_+ [blue (dark gray)] for up spin and v_- [orange (light gray)] for down spin. The dots mark the positions of the effective mass point and the spin tunneling is indicated by the gray dashed lines.

Figures 13(a)–13(c) present the situation of the conventional QRM, in the absence of the bias and the nonlinear interaction. Starting from the zero linear coupling $g_1 = 0$ in Fig. 13(a), the spin potentials are identical, with the effective particle staying at the origin where the potential minima are located. The increase of g_1 separates the potentials horizontally by $x_{0,\pm}$ while the potential values at the origin remain equal and invariant $v_+(0) = v_-(0) = 0$, as indicated in Fig. 13(b). However, with a linear coupling below g_s, the effective particle in the two spin components does not follow the potential separation but remains at the origin instead. This is because moving away from the origin would lose much of the negative tunneling energy due to the unequal spin weights in the potential difference, while staying at the origin keeps the maximum tunneling energy due to equal spin weights in the degenerate potentials. Increasing g_1 beyond

the critical point, the downward potential shift by b_0 enlarges the potential difference between the bottom and the origin as in Fig. 13(c), so that moving toward the potential bottom will gain more potential energy than the tunneling energy. Therefore the transition occurs and the particle leaves the origin. Note that either before or after the transition the spin distributions are spatially symmetric around the origin and the weights remain equal under spin exchange, thus the parity symmetry is preserved throughout.

Figures 13(d)–13(f) denote the situation of adding a bias to the linear coupling. A bias separates vertically the potentials of the up and down spins at $g_1 = 0$, as in Fig. 13(d), which breaks the spin balance and the parity symmetry from the beginning, thus being paramagnetic-like in polarization. In weak linear coupling regime, the bias moves the potential crossing point away from the origin which breaks the space inversion symmetry of the potential. However, the crossing point is moving to a higher potential which is not energetically favorable. So the parity symmetry is broken in both the spatial and spin parts. In a strong linear coupling beyond the critical point, as in Fig. 13(f), any strength of the bias will break the two-side balance maintained by the linear coupling in Fig. 13(c), thus a spontaneous symmetry breaking occurs. Note the state on each side is polarized due to the finite difference in spin-up and spin-down energy. Before the spontaneous symmetry breaking, the polarization or spin expectation $\langle \sigma_z \rangle$ cancels between the two sides. After the spontaneous symmetry breaking, without the two side cancellation, the polarization jumps to a finite value.

Figures 13(g)–13(i) show the situation of adding a nonlinear interaction to the linear coupling. The nonlinear interaction makes the frequency asymmetric between the up and down spins as in Fig. 13(g) and also shifts the spins in vertically opposite directions as in Fig. 13(h). However, the potential crossing always keeps invariant at the origin. Thus, the parity is well preserved even in the presence of a finite nonlinear interaction. Note that the vertical spin-dependent shift $b_\pm$ in Eq. (9) has an entangled form of the linear coupling g_1 and the nonlinear interaction g_2, increasing the nonlinear interaction at a fixed linear coupling will enlarge the vertical potential difference between the two spin directions. This vertical potential difference, in addition to b_0, will finally surpass the tunneling energy at the origin and lead to symmetry breaking with a first-order transition. So the polarization behavior is ferromagnetic-like. In a strong linear coupling beyond the g_s, also a tiny strength of nonlinear interaction will break the balance on the two sides in Fig. 13(c), leading to a spontaneous symmetry breaking from Fig. 13(c) to Fig. 13(i).

From the basic competitions discussed in the above one can also understand similarly the other mixed patterns of symmetry breaking.

B. Scaling of the Stark term

As mentioned around Eq. (2), the properties with the Stark-like term are similar by including the scaling factor, unless the frequency is high. We illustrate the scaling in Fig. 14 where it is shown that different Stark couplings under a fixed value of $\widetilde{g}_2 = (1 + \lambda)g_2$ have the same spin expectation and the same successive transition points (around $g_1/g_s \sim 1.0, 1.6, 2.6$).
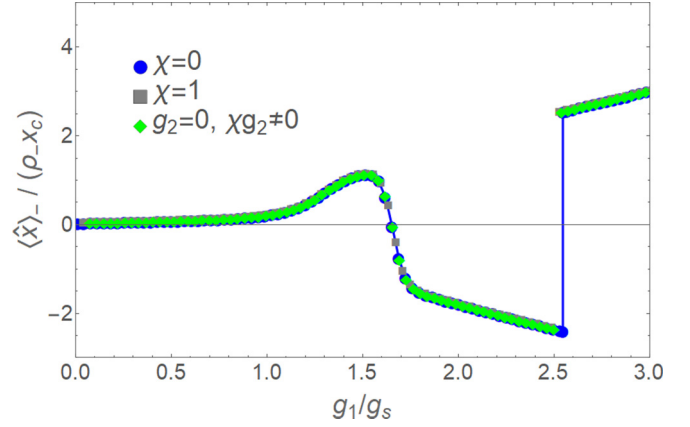
FIG. 14. Scaling of the Stark term. $\langle \hat{x}_- \rangle / (\rho_- x_c)$ versus g_1 with different Stark couplings $\chi = 0$ (blue dots), $\chi = 1$ (gray squares), and $g_2 = 0$, $\chi g_2 \neq 0$ (green diamonds) at a same value of $\widetilde{g}_2 = (1 + \chi)g_2$. Here $\omega = 0.1\Omega$, $\epsilon = 0.001 g_t$ and $\log[\widetilde{g}_2/g_t] = -4.5$.

This scaling can be simply understood from the semiclassical picture aforeformulated. In fact, from Eq. (7) we have seen that the potential displacement $x_{0,\pm}$, the effective bias $b_\pm$ and and the uniform shift b_0 are all functions of $\widetilde{g}_2' = (1 + \chi)g_2'$. It should be noted that, although the effective mass $m_\pm$ and $\varpi_\pm$, respectively, are not functions of $\widetilde{g}_2'$, their joint contribution in $v_\pm^{hp}$ is still a function of $\widetilde{g}_2'$ as

$$m_\pm \varpi_\pm^2 = \frac{\left[(1 \pm \chi g_2')^2 - g_2'^2 \right]}{(1 \mp g_2' \pm \chi g_2')} = (1 \pm \widetilde{g}_2'). \quad (28)$$

Namely, except for the kinetic term neglected in the semiclassical picture in the low-frequency limit, all contributions of the Stark-like term to $v_\pm$ can be scaled into a function of $\widetilde{g}_2'$. Thus, one will get the same phase diagrams for the presence of the Stark-like term by the scaling factor $(1 + \chi)$.

C. Full-quantum-mechanical effect for the successive transitions in the tricriticalities and tetracriticality

In the aforediscussed semiclassical picture there is no spatial structure of wave function or probability distribution over the effective spatial space. This simplification will miss some physics that becomes important at finite frequencies. Indeed, as described in Sec. IX, the successive transitions and tricriticalities emerge at a finite frequencies, which cannot be captured by the semiclassical picture. To understand these phenomena we shall fall back on a full-quantum-mechanical picture. By full-quantum-mechanical picture we refer to two points: first, not only the spin part but also the spatial part should be considered in quantum-mechanical picture; second, the spatial part is described by a wave function with wave-packet structure instead of a classical mass point. To include all the quantum states in one example we follow the wave function evolution in Figs. 12(c) and 12(d) where there are four quantum states. Accordingly, in Fig. 15, we sketch the spin potentials (upper panels) and the wave-function profiles (lower panels). The wave function is decomposed into left and right wave packets, as analyzed in a polaron-antipolaron picture [20] introduced in Sec. III B with Eq. (11), due to the barrier indicated in Fig. 2. Each wave packet is represented
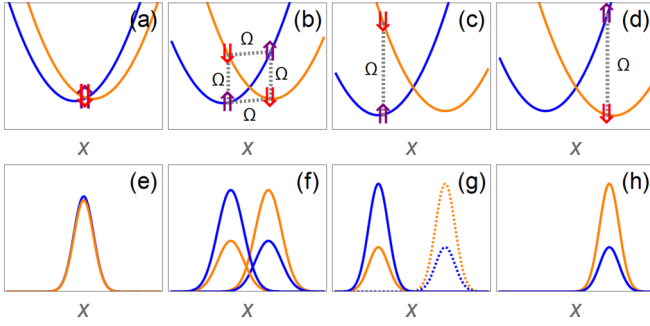
FIG. 15. Full-quantum-mechanical mechanisms for additional transition in successive transitions. (a–d) Effective potentials for the spin-up (blue) and spin-down (orange) components, the arrows represents the spins and gray dashed lines denotes the tunneling channels. (e–h) Schematic decomposed wave functions (plotted by amplitude) in the spin-up (blue) and spin-down (orange) components. The dashed lines in panel (g) show the vanishing left-right wave-packet overlap and indicate the disappearing wave packets.

by a displaced ground state of quantum harmonic oscillator [20,71] and the heights indicate the weights.

There are three transitions in the illustrated case, going through transitions I, III, and IV in Figs. 9(e) and 9(f). Before the first transition, the tunneling energy is dominating. As in Figs. 15(a) and 15(e), the single wave packets in both spins reside around the origin where the potential crossing point is located. The degeneracy at the crossing point yields equal weights of the two spin components. Both the single-wave-packet profiles and equal spin weights help to gain a maximum tunneling energy. The equal spin-component weight and the full overlapping yield a vanishing spin expectation $\langle \sigma_z \rangle$ and a saturation of $\langle \sigma_x \rangle$.

Transition-I: Increasing the linear coupling separates the potentials more and lower the potential bottoms, so that the potential energy comes to compete with the tunneling energy. After the first transition, as in Figs. 15(b) and 15(f), the wave function splits into four wave packets. Differently from the semiclassical picture there are now four channels of tunneling. The left-right tunneling arises due to the left-right overlaps of the wave packets, while the semiclassical particle has no such left-right overlap in any case. These left-right tunneling channels come to play an important role to balance potential asymmetry caused by the bias or the nonlinear interaction. Note in such a four-channel state, the polarizations of the two sides are canceling each other so that $\langle \sigma_z \rangle$ still remains almost vanishing at the presence of a weak bias and nonlinear interaction. Therefore, $\langle \sigma_z \rangle$ does not have an obvious change across the first transition thus the first transition leaves little imprint in $\langle \sigma_z \rangle$. However, the separated wave packets are moving away from the origin, the potential difference leads to unequal weights of the two spin components on each side. This weight difference lead to the reduction of spin flipping amplitude thus $\langle \sigma_x \rangle$ is decreasing in strength. As a result, $\langle \sigma_x \rangle$ is sensitive to the first transition and exhibits a critical behavior of second-order transition.

Transition-III: Further increase of g_1 will separate the wave packets more so that the left-right overlap becomes vanishing, as indicated in Fig. 15(g). Thus, the left-right channels of

tunneling in a vanishing strength cannot balance the potential asymmetry any more. As a result, the wave packets on the higher-potential side disappear and the second transition occurs. Note that at a higher frequency would have wider wave packets, thus the left-right overlap survive till larger g_1 and the transition occurs later. After this transition, the left-right cancellation does not exist in the one-side state so that $\langle \sigma_z \rangle$ jumps from a vanishing value to a finite value. Consequently this transition can find a clear signal in $\langle \sigma_z \rangle$. However, the state on the two sides have a similar amplitude of difference in the weights for the spin components. Note the strength of $\langle \sigma_x \rangle$ is decided by the weight difference of the two spins no matter which spin component has more weight. Thus, $\langle \sigma_x \rangle$ does not respond to this transition unless the potential asymmetry is large in the presence of strong bias and nonlinear interaction. Transition II has the same nature as transition III, although not present in the example of Fig. 15.

Transition-IV: An even larger g_1 will enhance much the entangled effective bias $b_\pm$ which is proportional to g_1^2. This enhanced bias will surpass the system bias ϵ which is originally stronger in small-g_1 regime. This strength reversion of the two competing biases ($b_\pm$ and ϵ) triggers transition IV. In principle, at the reversion the system should return to the four-wave-packet state. However, the left-right overlap is too small to maintain four-wave-packet state long enough to open a phase, unless the frequency is higher to get more-broadened wave packets. Hence, transition IV simply appears as one sharp transition. At a higher frequency the wave packets could be more broadened so that some left-right overlap could still remain, in such a situation transition IV could be bifurcated into two close transitions as mentioned for the tendency of four successive transitions in Sec. IX F. Since the state shifts from one side to the other, the sign of $\langle \sigma_z \rangle$ gets reversed so that $\langle \sigma_z \rangle$ exhibits a first-order change at this transition. In the same reason as in Transition-III $\langle \sigma_x \rangle$ still shows no sign at transition IV.

From the above understanding we see that $\langle \sigma_x \rangle$ can be sensitive to measure the first transition and $\langle \sigma_z \rangle$ is useful to track all the other transitions. The spin-filtered quantity $\langle a^\dagger + a \rangle_\pm / \rho_\pm$ is the spin displacement in our picture, i.e., the effective wave-packet position in each spin component. So it is naturally sensitive to the side shifting in transitions II, III, IV. Moreover, in the four-wave-packet state after transition I, each spin component has imbalanced weights of the left-side wave packet and the right-side wave packet, due to the potential difference within v_+ or v_- as shown in Fig. 15(b). Indeed $\langle a^\dagger + a \rangle_\pm / \rho_\pm$ reflects the effective mass center of each spin component, which is moving away from the origin after transition I. In consequence, $\langle a^\dagger + a \rangle_\pm / \rho_\pm$ is also responding to transition I, thus useful to detect all transitions simultaneously.

XIII. FINDING ANALYTIC BOUNDARIES

In previous Secs. VII–X we have given the analytic phase boundaries in the description of the phase diagrams. In Secs. in III C, XI, and XII we have got a basic understanding of the different transitions from the wave function changeovers and energy competitions. This would facilitate the finding

of analytic boundaries. Now we try to provide some brief derivations for the analytic phase boundaries.

A. Analytic boundaries in low-frequency limit

1. Analytic first-order boundaries

With the clarifications of the mechanisms for the transitions in the presence of the bias and the nonlinear interaction, we can extract the analytic phase boundaries. In the low-frequency limit, the boundary can be obtained from the semiclassical picture in Secs. III C and XII A. The energy minima can be available by minimization of the variational energy ε in Eq. (13) with respect to the position,

$$\frac{\partial}{\partial x}\varepsilon(x) = 0, \tag{29}$$

which gives three roots x_R, x_S, x_L from the right side to the left side, as indicated by Figs. 2(c)–2(e). The root x_S in the middle between the other two x_R, x_L on the right and left sides, respectively, is a saddle point which has a higher energy and does not enter the energy competition for the ground state. The transition boundary is then decided by

$$\varepsilon(x_R) = \varepsilon(x_L). \tag{30}$$

As mentioned in Sec. II, the bias is added to tune level difference for the qubit states in the two wells of the Josephson potential energy. So a relevant bias strength ϵ should be in a similar order of the potential well energy which is characterized by the frequency ω. Thus, in the low-frequency case, we can presume that ϵ is also small relatively to Ω. By keeping the leading order of ϵ/Ω in Eq. (30) we obtain

$$|g_{1c}| = g_s[1 + \frac{g_t\epsilon}{\tilde{g}_2\Omega}]\sqrt{1 - \tilde{g}_2^2/g_t^2}, \tag{31}$$

which gives Eqs. (16) and (17).

2. Critical point for ending of the first-order arc boundary

Note that, as mentioned for Fig. 4(d), in the regime of negative g_2, the above boundary Eq. (31) is an arc. Along this arc boundary the transition is of first order. At the ends of the arc the transition becomes second order and the first-order boundary closes at a critical point g_2^E. As revealed in Sec. III C, the first-order transition occurs in the presence of the energy saddle point x_S which separates two competing minima at x_R and x_L . Disappearing of the energy saddle will mean fading away of the first-order transition. The critical point comes with a flattened saddle. We show this saddle flattening in Fig. 16(a). Here, the green dashed line illustrates the minimum-saddle-minimum profile of the variational energy ε at a point along the first-order boundary, while the gray solid line shows the situation at the ends of the boundary where a flattened bottom can be clearly seen. This critical point can be figured out by vanishing of the first and second derivatives of the variational energy

$$\frac{\partial\varepsilon(x)}{\partial x} = 0, \quad \frac{\partial^2\varepsilon(x)}{\partial x^2} = 0. \tag{32}$$

It should be mentioned Eq. (32) is a necessary condition but not a sufficient one. We give an example by the blue dot-dashed line in Fig. 16(a), where the middle point of the
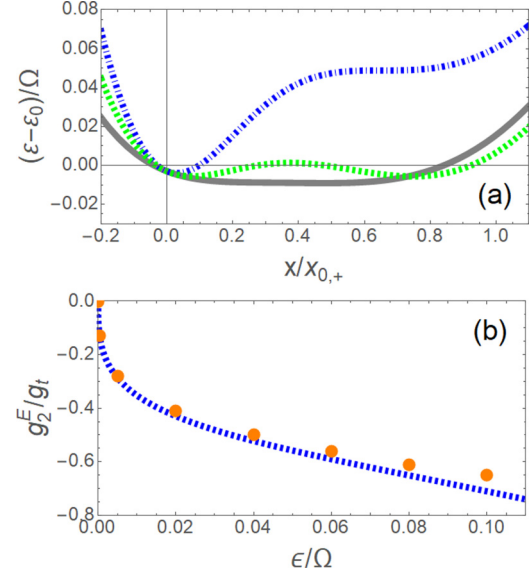
FIG. 16. Saddle point flattening and ending points of the first-order arc boundary. (a) Semiclassical variational energy at the end of the arc boundary $g_1 = 0.763g_s$, $g_2 = -0.554g_t$ (gray solid), in the arc $g_1 = 0.7g_s$, $g_2 = -0.665g_t$ (green dashed) and at an infection point $g_1 = 0.5g_s$, $g_2 = -0.81g_t$ (blue dot-dashed). Here $\epsilon = 10g_t$ and $\omega = 0.001\Omega$. (b) Critical value g_2^E at the end of the first-order arc boundary versus the bias ϵ from numerics (dots) and the analytic result (blue dashed).

shoulder shape fulfills Eq. (32) but it is an inflection point instead of a saddle point. Nevertheless, we can combine condition Eq. (32) and boundary Eq. (31) to extract the critical point,

$$g_2^E \approx 3\left(\frac{\epsilon}{5\Omega}\right)^{1/3} + \frac{226\epsilon}{75\Omega} - \frac{362\,011}{27\,000}\left(\frac{\epsilon}{5\Omega}\right)^{5/3}, \tag{33}$$

approximately for a weak bias and a nonlinear interaction. Figure 16(b) shows the above analytic g_2^E (dashed line) in comparison with the numerical ones (dots). It is interesting to see in the weak-bias regime g_2^E is in a fractional power law, which means g_2^E increases quickly with a small strength of the bias. So a small bias could break and open much the ring of the round boundary in Fig. 4(b).

B. Analytic boundaries for the successive transitions at finite frequencies

Based on the physical picture analyzed in Sec. XII C we can obtain the phase boundaries in the tricritical scenarios at finite frequencies. As depicted in Fig. 15(b), there are four channels of tunneling including same-side ones and left-right ones, respectively. Unlike in the semiclassical picture, now the left and right states can simultaneously get involved in a ground state via left-right tunneling. Note in a strong coupling around the transitions the same-side tunneling is dominating while the left-right tunneling is much weaker. Thus, we can decompose the wave function into right (R) and left (L) states $|\Psi\rangle = c_R|\psi_R\rangle + c_L|\psi_L\rangle$, up to a normalization factor, and

take the left-right tunneling as an perturbation. The right and left states, respectively, consist of two spin components,

$$|\psi_{\rm L}\rangle = \alpha^+ \varphi_\alpha^+ |\uparrow\rangle + \beta^- \varphi_\beta^- |\downarrow\rangle, \qquad (34)$$

$$|\psi_{\rm R}\rangle = \alpha^- \varphi_\alpha^- |\downarrow\rangle + \beta^+ \varphi_\beta^+ |\uparrow\rangle, \qquad (35)$$

where $\alpha^\pm, \beta^\pm$ represent the weight coefficient of the wave packet $\varphi_j^\pm \in \{\varphi_\alpha^+, \varphi_\beta^-, \varphi_\alpha^-, \varphi_\beta^+\}$ and for the ground state they have opposite signs for different spins. Now we can defined the tunneling energy $\Omega_{ij} = w_{i\bar{j}} \frac{\Omega}{2} S_{i\bar{j}}$ for the same-side ones ($\Omega_{\alpha\beta}$ and $\Omega_{\beta\alpha}$) and left-right ones ($\Omega_{\alpha\alpha}$ and $\Omega_{\beta\beta}$), as $\varphi_\alpha^+, \varphi_\beta^-$ are on a same side (left) and $\varphi_\alpha^-, \varphi_\beta^+$ are on the other same side (right). Here $w_{i\bar{j}}$ is the weight product of $\alpha^\pm$ and $\beta^\pm$. Note in Ω_{ij} the wave-packet overlap $S_{i\bar{j}} = \langle \varphi_i^+ | \varphi_j^- \rangle$ involves opposite spins.

The right and left states, respectively, are formed in the same-side tunneling $\Omega_{\alpha\beta}$ and $\Omega_{\alpha\beta}$. The left state is decided by the lower eigenstate of the matrix equation

$$\begin{pmatrix} h_{\beta\beta}^- & \frac{1}{2} S_{\alpha\bar{\beta}} \Omega \\ \frac{1}{2} S_{\alpha\bar{\beta}} \Omega & h_{\alpha\alpha}^+ \end{pmatrix} \begin{pmatrix} \beta^- \\ \alpha^+ \end{pmatrix} = \varepsilon_{\rm L} \begin{pmatrix} \beta^- \\ \alpha^+ \end{pmatrix}, \qquad (36)$$

where $h_{ij}^\pm = \langle \varphi_i^\pm | (h^\pm - b_0 - \varepsilon_0) | \varphi_j^\pm \rangle$ and the irrelevant constants b_0, ε_0 have been substracted. One can get the right state similarly. The corresponding energy can be easily obtained as

$$\varepsilon_{\rm L} = \frac{1}{2} \Big[(h_{\beta\beta}^- + h_{\alpha\alpha}^+) - \sqrt{(h_{\beta\beta}^- - h_{\alpha\alpha}^+)^2 + S_{\alpha\bar{\beta}}^2 \Omega^2} \Big], \qquad (37)$$

$$\varepsilon_{\rm R} = \frac{1}{2} \Big[(h_{\beta\beta}^+ + h_{\alpha\alpha}^-) - \sqrt{(h_{\beta\beta}^+ - h_{\alpha\alpha}^-)^2 + S_{\beta\bar{\alpha}}^2 \Omega^2} \Big]. \qquad (38)$$

The wave packet $\varphi_j^\pm$ can be well approximated by the displaced ground state of quantum harmonic oscillator, with the displacement $\zeta_{i,\pm} x_{0,\pm}$ ($i = \alpha, \beta$) renormalized from the position of the potential bottom $x_{0,\pm}$[20]. Explicitly we have

$$h_{ii}^\pm = \frac{\omega}{2} \left\{ \varpi_\pm - \frac{[1 - (1 - \zeta_{i,\pm})^2] g_1'^2}{(1 \pm \widetilde{g_2})} \right\} \mp \epsilon, \qquad (39)$$

and $S_{\alpha\bar{\beta}} \approx S_{\beta\bar{\alpha}} \approx 1$ in gaining the maximum tunneling energy. The successive transitions occur in weak bias ϵ and nonlinear interaction g_2, in such situations the displacements can be approximated by those of the conventional QRM. Thus, in the leading order, the energy difference of the left and right states reads

$$\varepsilon_{\rm L} - \varepsilon_{\rm R} = \bar{g}_2 \bar{g}_1^2 \zeta^2 \left[\frac{(1 + \zeta/2)}{\sqrt{(\zeta^2 + \bar{g}_1^{-4})}} - 1 \right] \Omega - \frac{2\zeta\epsilon}{\sqrt{(\zeta^2 + \bar{g}_1^{-4})}}, \qquad (40)$$

where we have applied $\zeta_{i,\pm} \approx \zeta$ and $\zeta = (1 - \bar{g}_1^{-4})^{1/2}$ is the displacement renormalization from the conventional QRM [20].

Standing in a phase of the two-branch state described in Sec. XI and Figs. 15(b)–15(f), we can judge the onset of the transitions to broken-branch states by an exponential decay of the state weight on one side, $\delta_c = (c_{\rm R}/c_{\rm L})^{\pm 1} \sim e^{-1}$, where ± 1 depends on which broken-branch state the system is transiting to. Exactly speaking, there is a transition width due to the process of weight shifting. Nevertheless, this transition width is quite narrow as the right-left wave-packet overlap is

decaying exponentially. Setting $\delta_c \sim e^{-1}$ is within this narrow transition width, thus being a good approximation to represent the transition boundary. Thus, at the transition we can treat by a perturbation from the left-right tunneling energy ($\Omega_{\alpha\alpha}$, $\Omega_{\beta\beta}$) as well as the single-particle left-right overlap energy ($t_{\alpha\beta}^+, t_{\beta\alpha}^-$)

$$\delta_c = (\Omega_{\alpha\alpha} + \Omega_{\beta\beta} + t_{\alpha\beta}^+ + t_{\beta\alpha}^-)/[\eta_{\rm LR}(\varepsilon_{\rm L} - \varepsilon_{\rm R})], \qquad (41)$$

where we have defined $t_{ij}^\pm = w_{ij} h_{ij}^\pm$ and $\eta_{\rm LR} = \pm 1$ is decided by which side of state has a lower energy. With the aforementioned approximation for $\varphi_j^\pm$ and $\zeta_{i,\pm}$, in the leading order, we get

$$\Omega_{\alpha\alpha} + \Omega_{\beta\beta} \approx -\frac{\Omega}{2} S_{\alpha\bar{\alpha}}, \qquad (42)$$

$$t_{\alpha\beta}^+ + t_{\beta\alpha}^- \approx \alpha\beta \left[\omega + (1 - \zeta)^2 \bar{g}_1^2 \frac{\Omega}{2} \right] S_{\alpha\beta}, \qquad (43)$$

where $S_{\alpha\beta} \approx S_{\beta\alpha} \approx S_{\alpha\bar{\alpha}} \approx S_{\beta\bar{\beta}} \approx \exp[-\zeta^2 \bar{g}_1^2 \Omega/(2\omega)]$ is approximate left-right wave-packet overlap, and the weight coefficients $\alpha^\pm \approx \pm\alpha$, $\beta^\pm \approx \pm\beta$, with $\alpha = \sqrt{(1+\zeta)/2}$, $\beta = \sqrt{(1-\zeta)/2}$, are the leading contributions from the conventional QRM [20]. For $\Omega_{\alpha\alpha} + \Omega_{\beta\beta}$ we have used $\alpha^2 + \beta^2 = 1$. It should be noted here that, unlike the opposite spins in $S_{\alpha\bar{\alpha}} = \langle \varphi_\alpha^+ | \varphi_\alpha^- \rangle$, the wave-packet overlap $S_{\alpha\beta} = \langle \varphi_\alpha^+ | \varphi_\beta^+ \rangle$ involves the same spin thus also being a left-right overlap, as indicated by Eqs. (34) and (35).

Combining Eqs. (40)–(43), we get the analytic expressions for boundaries II and III,

$$\widetilde{g}_{2c}^{\rm II,III} = \pm \frac{(1-t)g_t}{\delta_c \zeta^3 \bar{g}_1^2} \exp\left[-\frac{\zeta^2 \bar{g}_1^2 \Omega}{2\omega} \right] + \frac{4\epsilon}{\zeta^2 \bar{g}_1^2 \Omega} g_t. \qquad (44)$$

Transition-IV is the shifting between pure left state and pure right state, thus setting $\varepsilon_{\rm L} - \varepsilon_{\rm R} = 0$ we find

$$\widetilde{g}_{2c}^{\rm IV} = \frac{4\epsilon}{\zeta^2 \bar{g}_1^2 \Omega} g_t + O\left[\left(\frac{\epsilon}{\Omega}\right)^3 \right]. \qquad (45)$$

As we have seen from Figs. 6, 7, 9, 10, and 11 in Sec. IX, these analytic boundaries work quite well in comparisons with the numerics.

XIV. CONCLUSIONS AND DISCUSSIONS

By combining exact diagonalization and analytic methods in a semiclassical picture and a full quantum-mechanical picture, we have presented a thorough study on the ground state of the quantum Rabi model in the presence of the bias and the nonlinear interaction. The model exhibits different patterns of symmetry breaking, including the paramagnetic-like, antiferromagnetic like, spontaneous symmetry breaking, paramagnetic-like plus first- or second-order transitions, antiferromagnetic-like plus first- or second-order transitions. These symmetry-breaking patterns bring a rich and colorful world of phase diagrams. We have obtained the full phase diagrams and the analytic phase boundaries, both in the low-frequency limit and at finite frequencies. Various situations for the occurrence of tricriticality are unveiled, respectively: (i) induced by the competition of the linear coupling and nonlinear interaction in the presence of the bias, in the low-frequency limit. (ii) induced by raising the frequency in the

respective presence of the nonlinear interaction or the bias. (iii) induced by the competition of linear coupling with the nonlinear interaction or the bias, under fixed finite frequencies. We also show two situations for tricriticality coexisting with another triple point, respectively, labeled by (iv), which is induced by the interplay of linear coupling with both the nonlinear interaction and the bias under fixed finite frequencies, and (v), which is induced by varying the frequency in the interplay of the nonlinear interaction and the bias. The system could have four different quantum phases, we have revealed that all four phases can meet to form a quadruple point and tetracriticality. The low-frequency-limit phase boundary of nonlinear interaction in the absence of bias turns out to be a quadruple line. In comparison with the semiclassical low-frequency limit, the finite frequencies lead to more phase transitions. By analyzing the energy competitions and monitoring the essential changes of quantum states in the transitions, we have clarified the semiclassical and quantum-mechanical mechanisms underlying the aforementioned phenomena. We see that the full quantum-mechanical effect leads to much richer physics than the semiclassical picture, including additional phase transitions, tricriticalities, and formation of quadruple points as well as a fine structure of spontaneous symmetry breaking.

Note that the model we consider can be implemented in the experimental setups as in the superconducting circuit system [56,68]. It is convenient to cool the superconducting circuits down to the ground state. The model parameters are controllable as the superconducting systems are composed of LC circuits of which the frequency parameters are quite tunable. It is worthwhile to give an estimation on the regime of experimental parameters that is favorable for detections of the phenomena we address in the present work, such as successive transitions and tricricalities. The symmetry-breaking patterns, second- or first-order transitions and tricriticality-(i) in the low-frequency limit are illustrated at frequencies of order $\omega = 0.001 \sim 0.01\Omega$, while the nonlinear interaction g_2 has an order similar to ω and the bias is in a range of order around $\epsilon = 0 \sim 10\omega$. A typical experimental strength for the tunneling strength Ω is of order 10 GHz [72] in superconducting circuit systems, although the order can reach 50 GHz

in microwave cavities and even 350 THz in optical cavities. For the superconducting systems we are more concerned, the frequency $\omega = 0.001 \sim 0.01\Omega$ corresponds to the order $10 \sim 100$ MHz. The additional transitions and the tricricalities occur at the finite frequencies of order around $\omega = 0.1 \sim 1\Omega$, while ϵ and g_2 are illustrated in a range of $10^{-5} \sim 10^{-1}g_t$ where g_t is of the same order of ω. In LC circuits these parameters would correspond to $\omega = 1 \sim 10$ GHz and ϵ, $g_2 = 10^{-2} \sim 10^3$ MHz. These parameter regimes would open a wide window accessible for the circuit systems.

Our results would be relevant for the growing interest in the nonlinear effect [23,24,56,58,59,64–68,73,74] in the context of continuing enhancements of experimental light-matter couplings [1,43–50,52–54]. Our analytic phase boundaries and physical analysis may provide some convenience and insights. The various situations for the occurrence of tricriticality and tetracriticality unveiled here also give a paradigmatic illustration for a single-qubit system exhibiting a rich phenomenology of multicriticality. Similar analysis shows that other realistic conditions, such as the presence of anisotropy, can also bring multicriticality [75]. It should be mentioned that tricriticality and multicriticality are of broad interest in physics, e.g., tricritical behavior can be also observed in Bose-Einstein condensates in cold atoms [76]. Interestingly the Hamiltonian of the quantum Rabi model with anisotropy can be mapped to a model with Rashba spin-orbit coupling [75] which has some similarities with the single-particle Hamiltonian of spin-orbit coupled two-component Bose-Einstein condensates [76] and Rashba spin-orbit coupling nanowires [77–79]. Thus, we speculate that our analysis might also provide some insights for possible extended applications in cold atoms and nanowires. As a final remark, we think the phenomena revealed in this work concerning nonlinearity might also leave imprints in the Bloch-Siegert effect [80] and dynamics [12,19,81], which we shall discuss in some other works.

[1] P. Forn-Díaz, L. Lamata, E. Rico, J. Kono, and E. Solano, Rev. Mod. Phys. **91**, 025005 (2019).

[2] D. Braak, Phys. Rev. Lett. **107**, 100401 (2011).

[3] A. Le Boité, Adv. Quantum Technol. **3**, 1900140 (2020).

[4] A. F. Kockum, A. Miranowicz, S. De Liberato, S. Savasta, and F. Nori, Nat. Rev. Phys. **1**, 19 (2019).

[5] E. T. Jaynes and F. W. Cummings, Proc. IEEE **51**, 89 (1963).

[6] I. I. Rabi, Phys. Rev. **51**, 652 (1937).

[7] G. Romero, D. Ballester, Y. M. Wang, V. Scarani, and E. Solano, Phys. Rev. Lett. **108**, 120501 (2012).

[8] R. Stassi and F. Nori, Phys. Rev. A **97**, 033823 (2018).

[9] R. Stassi, M. Cirio, and F. Nori, npj Quantum Inf. **6**, 67 (2020).

[10] V. Macrì, F. Nori, and A. F. Kockum, Phys. Rev. A **98**, 062327 (2018).

[11] J. S. Pedernales, M. Beau, S. M. Pittman, I. L. Egusquiza, L. Lamata, E. Solano, and A. del Campo, Phys. Rev. Lett. **120**, 160403 (2018).

[12] F. A. Wolf, M. Kollar, and D. Braak, Phys. Rev. A **85**, 053817 (2012).

[13] E. Solano, Physics **4**, 68 (2011).

[14] Q.-H. Chen, C. Wang, S. He, T. Liu, and K.-L. Wang, Phys. Rev. A **86**, 023822 (2012).

[15] E. K. Irish and J. Gea-Banacloche, Phys. Rev. B **89**, 085421 (2014).

[16] J. Larson and E. K. Irish, J. Phys. A: Math. Theor. **50**, 174002 (2017).

[17] Q.-T. Xie, S. Cui, J.-P. Cao, L. Amico, and H. Fan, Phys. Rev. X **4**, 021046 (2014).

[18] M. T. Batchelor and H.-Q. Zhou, Phys. Rev. A **91**, 053808 (2015).

[19] M.-J. Hwang, R. Puebla, and M. B. Plenio, Phys. Rev. Lett. **115**, 180404 (2015).

[20] Z.-J. Ying, M. Liu, H.-G. Luo, H.-Q. Lin, and J. Q. You, Phys. Rev. A **92**, 053823 (2015).

[21] M. Liu, S. Chesi, Z.-J. Ying, X. Chen, H.-G. Luo, and H.-Q. Lin, Phys. Rev. Lett. **119**, 220601 (2017).

[22] L. Cong, X.-M. Sun, M. Liu, Z.-J. Ying, and H.-G. Luo, Phys. Rev. A **95**, 063803 (2017).

[23] L. Cong, X.-M. Sun, M. Liu, Z.-J. Ying, and H.-G. Luo, Phys. Rev. A **99**, 013815 (2019).

[24] Z.-J. Ying, L. Cong, and X.-M. Sun, J. Phys. A: Math. Theor. **53**, 345301 (2020).

[25] M. Liu, Z.-J. Ying, J.-H. An, and H.-G. Luo, New J. Phys. **17**, 043001 (2015).

[26] M. Liu, Z.-J. Ying, J.-H. An, H.-G. Luo, and H.-Q. Lin, J. Phys. A: Math. Theor. **50**, 084003 (2017).

[27] S. Ashhab, Phys. Rev. A **87**, 013826 (2013).

[28] L. Yu, S. Zhu, Q. Liang, G. Chen, and S. Jia, Phys. Rev. A **86**, 015803 (2012).

[29] T. Liu, M. Feng, W. L. Yang, J. H. Zou, L. Li, Y. X. Fan, and K. L. Wang, Phys. Rev. A **88**, 013820 (2013).

[30] Y.-Y. Zhang, Phys. Rev. A **94**, 063824 (2016).

[31] Y. Wang, W.-L. You, M. Liu, Y.-L. Dong, H.-G. Luo, G. Romero, and J. Q. You, New J. Phys. **20**, 053061 (2018).

[32] L.-T. Shen, Z.-B. Yang, H.-Z. Wu, and S.-B. Zheng, Phys. Rev. A **95**, 013819 (2017).

[33] F. H. Maldonado-Villamizar, C. Huerta Alderete, and B. M. Rodríguez-Lara, Phys. Rev. A **100**, 013811 (2019).

[34] L. Cong, S. Felicetti, J. Casanova, L. Lamata, E. Solano, and I. Arrazola, Phys. Rev. A **101**, 032350 (2020).

[35] Q. Xie, H. Zhong, M. T. Batchelor, and C. Lee, J. Phys. A: Math. Theor. **50**, 113001 (2017).

[36] H. Zhong, Q. Xie, M. T. Batchelor, and C. Lee, J. Phys. A: Math. Theor. **46**, 415302 (2013).

[37] H.-P. Eckle and H. Johannesson, J. Phys. A: Math. Theor. **50**, 294004 (2017).

[38] V. Penna, F. A. Raffa, and R. Franzosi, J. Phys. A: Math. Theor. **51**, 045301 (2017).

[39] A. J. Maciejewski and T. Stachowiak, J. Phys. A: Math. Theor. **52**, 485303 (2019).

[40] Y.-F. Xie, L. Duan, and Q.-H. Chen, J. Phys. A: Math. Theor. **52**, 245304 (2019).

[41] C. Sánchez Muñoz, A. Frisk Kockum, A. Miranowicz, and F. Nori, Phys. Rev. A **102**, 033716 (2020).

[42] K. K. W. Ma, Phys. Rev. A **102**, 053709 (2020).

[43] A. Wallraff, D. I. Schuster, A. Blais, L. Frunzio, R.-S. Huang, J. Majer, S. Kumar, S. M. Girvin, and R. J. Schoelkopf, Nature **431**, 162 (2004).

[44] G. Günter, A. A. Anappara, J. Hees, A. Sell, G. Biasiol, L. Sorba, S. De Liberato, C. Ciuti, A. Tredicucci, A. Leitenstorfer, and R. Huber, Nature **458**, 178 (2009).

[45] T. Niemczyk, F. Deppe, H. Huebl, E. P. Menzel, F. Hocke, M. J. Schwarz, J. J. Garcia-Ripoll, D. Zueco, T. Hümmer, E. Solano, A. Marx, and R. Gross, Nat. Phys. **6**, 772 (2010).

[46] B. Peropadre, P. Forn-Díaz, E. Solano, and J. J. García-Ripoll, Phys. Rev. Lett. **105**, 023601 (2010).

[47] P. Forn-Díaz, J. García-Ripoll, B. Peropadre, J.-L. Orgiazzi, M. Yurtalan, R. Belyansky, C. Wilson, and A. Lupascu, Nat. Phys. **13**, 39 (2017).

[48] P. Forn-Díaz, J. Lisenfeld, D. Marcos, J. J. García-Ripoll, E. Solano, C. J. P. M. Harmans, and J. E. Mooij, Phys. Rev. Lett. **105**, 237001 (2010).

[49] G. Scalari, C. Maissen, D. Turčinková, D. Hagenmüller, S. De Liberato, C. Ciuti, C. Reichl, D. Schuh, W. Wegscheider, M. Beck, and J. Faist, Science **335**, 1323 (2012).

[50] Z.-L. Xiang, S. Ashhab, J. Q. You, and F. Nori, Rev. Mod. Phys. **85**, 623 (2013).

[51] J. Q. You and F. Nori, Phys. Rev. B **68**, 064509 (2003).

[52] F. Yoshihara, T. Fuse, S. Ashhab, K. Kakuyanagi, S. Saito, and K. Semba, Nat. Phys. **13**, 44 (2017).

[53] F. Yoshihara, T. Fuse, S. Ashhab, K. Kakuyanagi, S. Saito, and K. Semba, Phys. Rev. A **95**, 053824 (2017).

[54] X. Gu, A. F. Kockum, A. Miranowicz, Y. xi Liu, and F. Nori, Phys. Rep. **718–719**, 1 (2017).

[55] S. Ashhab and F. Nori, Phys. Rev. A **81**, 042311 (2010).

[56] S. Felicetti, D. Z. Rossatto, E. Rico, E. Solano, and P. Forn-Díaz, Phys. Rev. A **97**, 013851 (2018).

[57] S. Felicetti, M.-J. Hwang, and A. Le Boité, Phys. Rev. A **98**, 053859 (2018).

[58] S. Felicetti, J. S. Pedernales, I. L. Egusquiza, G. Romero, L. Lamata, D. Braak, and E. Solano, Phys. Rev. A **92**, 033817 (2015).

[59] R. Puebla, M.-J. Hwang, J. Casanova, and M. B. Plenio, Phys. Rev. A **95**, 063844 (2017).

[60] I. Travěnec, Phys. Rev. A **85**, 043805 (2012).

[61] C. F. Lo, K. L. Liu, and K. M. Ng, Europhys. Lett. **42**, 1 (1998).

[62] L. Duan, Y.-F. Xie, D. Braak, and Q.-H. Chen, J. Phys. A: Math. Theor. **49**, 464002 (2016).

[63] L. Garbe, I. L. Egusquiza, E. Solano, C. Ciuti, T. Coudreau, P. Milman, and S. Felicetti, Phys. Rev. A **95**, 053854 (2017).

[64] J. Casanova, R. Puebla, H. Moya-Cessa, and M. B. Plenio, npj Quantum Inf. **4**, 47 (2018).

[65] Y.-F. Xie, L. Duan, and Q.-H. Chen, Phys. Rev. A **99**, 013809 (2019).

[66] J. Peng, E. Rico, J. Zhong, E. Solano, and I. L. Egusquiza, Phys. Rev. A **100**, 063820 (2019).

[67] S. Felicetti and A. Le Boité, Phys. Rev. Lett. **124**, 040404 (2020).

[68] P. Bertet, I. Chiorescu, C. J. P. M. Harmans, and J. E. Mooij, arXiv:cond-mat/0507290.

[69] P. Bertet, I. Chiorescu, G. Burkard, K. Semba, C. J. P. M. Harmans, D. P. DiVincenzo, and J. E. Mooij, Phys. Rev. Lett. **95**, 257002 (2005).

[70] J. E. Mooij, T. P. Orlando, L. Levitov, L. Tian, C. H. van der Wal, and S. Lloyd, Science **285**, 1036 (1999).

[71] S. Bera, S. Florens, H. U. Baranger, N. Roch, A. Nazir, and A. W. Chin, Phys. Rev. B **89**, 121108(R) (2014).

[72] A. Blais, R.-S. Huang, A. Wallraff, S. M. Girvin, and R. J. Schoelkopf, Phys. Rev. A **69**, 062320 (2004).

[73] R. Puebla, J. Casanova, O. Houhou, E. Solano, and M. Paternostro, Phys. Rev. A **99**, 032303 (2019).

[74] Z. Lü, C. Zhao, and H. Zheng, J. Phys. A: Math. Theor. **50**, 074002 (2017).

[75] Z.-J. Ying, arXiv:2010.15113.

[76] Y. Li, L. P. Pitaevskii, and S. Stringari, Phys. Rev. Lett. **108**, 225301 (2012).

[77] F. Nagasawa, D. Frustaglia, H. Saarikoski, K. Richter, and J. Nitta, Nat. Commun. **4**, 2526 (2013).

[78] Z.-J. Ying, P. Gentile, C. Ortix, and M. Cuoco, Phys. Rev. B **94**, 081406(R) (2016).

[79] Z.-J. Ying, M. Cuoco, C. Ortix, and P. Gentile, Phys. Rev. B **96**, 100506(R) (2017).

[80] I. Pietikäinen, S. Danilin, K. S. Kumar, A. Vepsäläinen, D. S. Golubev, J. Tuorila, and G. S. Paraoanu, Phys. Rev. B **96**, 020501(R) (2017).

[81] A. Crespi, S. Longhi, and R. Osellame, Phys. Rev. Lett. **108**, 163601 (2012).